

**OPEN ACCESS**

## Role of the Microstructure in the Li-Storage Performance of Spinel-Structured High-Entropy (Mn,Fe,Co,Ni,Zn) Oxide Nanofibers

To cite this article: Claudia Triolo *et al* 2024 *J. Electrochem. Soc.* **171** 060509

View the [article online](#) for updates and enhancements.

### You may also like

- [Theoretical Study on The Adsorption of NO on Metal Macrocycles, Metal=Mn,Fe,Co,Ni,Cu,Zn](#)  
Tien Quang Nguyen, Allan Abraham Bustria Padama, Mary Clare Sison Escano et al.
- [Multiferroic approach for Cr,Mn,Fe,Co,Ni,Cu substituted BaTiO<sub>3</sub> nanoparticles](#)  
Kuldeep Chand Verma and R K Kotnala
- [The effect of Cu/M \(M=Mn,Co,Ni,Zn\) substitution upon superconductivity in Nd<sub>1-x</sub>Ce<sub>x</sub>Co<sub>4</sub>CuO<sub>4</sub>](#)  
G Hilscher, M Forsthuber, S Pollinger et al.

## Your Lab in a Box!

The PAT-Tester-i-16: All you need for Battery Material Testing.

- ✓ **All-in-One Solution with Integrated Temperature Chamber (10-80°C)!**  
No additional devices are required to measure at a stable ambient temperature.
- ✓ **Fully featured Multichannel Potentiostat / Galvanostat / EIS!**  
Up to sixteen independent battery test channels, no multiplexing.
- ✓ **Ideally suited for High-Precision Coulometry!**  
Measure with excellent accuracy and signal-to-noise ratio at the same time.
- ✓ **Small Footprint, Easy to Setup and Operate!**  
Cableless connection of 3-electrode battery test cells. Full multi-user, multi-device control via LAN.

**EL-CELL**<sup>®</sup>  
electrochemical test equipment



Learn more on our product website:



Download the Data Sheet (PDF):



Or contact us directly:









+49 40 79012-734

sales@el-cell.com

www.el-cell.com



# Role of the Microstructure in the Li-Storage Performance of Spinel-Structured High-Entropy (Mn,Fe,Co,Ni,Zn) Oxide Nanofibers

Claudia Triolo,<sup>1,2</sup>  Mariam Maisuradze,<sup>2,3</sup>  Yanchen Liu,<sup>4</sup> Min Li,<sup>2,3</sup> Gioele Pagot,<sup>2,5</sup>   
Alessandro Ponti,<sup>6</sup>  Vito Di Noto,<sup>2,3</sup>  Giuliana Aquilanti,<sup>7</sup> Nicola Pinna,<sup>4,z</sup>   
Marco Giorgetti,<sup>2,3,z</sup>  and Saveria Santangelo<sup>1,2,z</sup> 

<sup>1</sup>Dipartimento di Ingegneria Civile, dell'Energia, dell'Ambiente e dei Materiali (DICEAM), Università "Mediterranea," 89122 Reggio Calabria, Italy

<sup>2</sup>National Reference Center for Electrochemical Energy Storage (GISEL), Consorzio Interuniversitario Nazionale per la Scienza e Tecnologia dei Materiali (INSTM), 50121 Firenze, Italy

<sup>3</sup>Department of Industrial Chemistry "Toso Montanari," University of Bologna, 40136, Bologna, Italy

<sup>4</sup>Department of Chemistry & The Center for the Science of Materials Berlin, Humboldt-Universität zu Berlin, 12489 Berlin, Germany

<sup>5</sup>Department of Industrial Engineering, Section of Chemistry for the Technology (ChemTech), University of Padova, 35131 Padova (PD), Italy

<sup>6</sup>Laboratorio di Nanotecnologie, Istituto di Scienze e Tecnologie Chimiche "Giulio Natta" (SCITEC), Consiglio Nazionale delle Ricerche, 20138 Milano, Italy

<sup>7</sup>Elettra Sincrotrone Trieste S.C.p.A., 34149 Basovizza, Trieste, Italy

High-entropy oxides with spinel structure (SHEOs) are promising anode materials for next-generation lithium-ion batteries (LIBs). In this work, electrospun (Mn,Fe,Co,Ni,Zn) SHEO nanofibers produced under different conditions are evaluated as anode materials in LIBs and thoroughly characterised by a combination of analytical techniques. The variation of metal load (19.23 or 38.46 wt% relative to the polymer) in the precursor solution and of calcination conditions (700 °C/0.5 h, or 700 °C/2 h followed by 900 °C/2 h) affects the morphology, microstructure, crystalline phase, and surface composition of the pristine SHEO nanofibers and the resulting electrochemical performance, whereas mechanism of Li<sup>+</sup> storage does not substantially change. Causes of long-term (>650 cycles) capacity fading are elucidated via ex situ synchrotron X-ray absorption spectroscopy. The results evidence that the larger amounts of Fe, Co, and Ni cations irreversibly reduced to the metallic form during cycling are responsible for faster capacity fading in nanofibers calcined under milder conditions. The microstructure of the active material plays a key role. Nanofibers composed by larger and better-crystallized grains, where a stable solid/electrolyte interphase forms, exhibit superior long-term stability (453 mAh g<sup>-1</sup> after 550 cycles at 0.5 A g<sup>-1</sup>) and rate-capability (210 mAh g<sup>-1</sup> at 2 A g<sup>-1</sup>).

© 2024 The Author(s). Published on behalf of The Electrochemical Society by IOP Publishing Limited. This is an open access article distributed under the terms of the Creative Commons Attribution Non-Commercial No Derivatives 4.0 License (CC BY-NC-ND, <http://creativecommons.org/licenses/by-nc-nd/4.0/>), which permits non-commercial reuse, distribution, and reproduction in any medium, provided the original work is not changed in any way and is properly cited. For permission for commercial reuse, please email: [permissions@iopublishing.org](mailto:permissions@iopublishing.org). [DOI: [10.1149/1945-7111/ad51aa](https://doi.org/10.1149/1945-7111/ad51aa)]



Manuscript submitted February 4, 2024; revised manuscript received May 13, 2024. Published June 7, 2024.

Supplementary material for this article is available [online](#)

The energy transition to limit climate changes has led to the expansion of the electric vehicle market, in which lithium ion batteries (LIBs) have wide application thanks to their excellent charge storage performance and low maintenance costs. The need to further increase the energy density and long-term cycling stability (LTS) of LIBs has promoted the search for new electrode materials. Graphite, which is nowadays the most used anode, possesses low specific capacity (372 mAh g<sup>-1</sup>) and therefore struggles to meet the current requirements for the energy storage systems. As an alternative, the Li metal anode has attractive properties, such as much higher specific capacity of 3860 mAh g<sup>-1</sup> and lower negative electrochemical potential of -3.04 V vs SHE.<sup>1</sup> However, dendrite formation is a huge problem for this material, as it leads not only to low Coulombic efficiency (CE) and capacity decay,<sup>2-6</sup> but is a serious safety risk. Short-circuiting can produce large amount of heat, and even explosion.<sup>7</sup> The formation of a thick solid/electrolyte interphase (SEI) and, the ensuing volume change are additional issue that hinder the utilisation of this material.<sup>8</sup> Another extensively studied anode is Si (with a specific capacity of 4200 mAh g<sup>-1</sup>,<sup>9,10</sup>) but its volume variation greater than 300%, as well as an unstable SEI, where Li trapping might occur, inevitably leads to low CE and capacity loss. Slow kinetics and low conductivity are also noteworthy issues.<sup>9,11-13</sup> Si/C-based anodes, proposed in recent years to

overcome the drawbacks of silicon, are an undeniable improvement, but the CE still generally fails to reach values high enough to satisfy the demands of commercial applications. Moreover, since obtaining a protective layer of Si/C distributed homogeneously on the Si anode is not easy, the volume expansion of Si cannot be completely avoided, again leading to poor electrochemical performance.<sup>14</sup> Additionally, the Si/C layers could react with lithium ions and consequently decompose into Si and C, thus losing the protective ability.<sup>15,16</sup> Among other alternative anode materials, there are classic titanium-based insertion-type metal oxide anodes, such as TiO<sub>2</sub><sup>17</sup> and Li<sub>4</sub>Ti<sub>5</sub>O<sub>12</sub>.<sup>18-20</sup> However, their high mass and relatively limited uptake of lithium make these materials more useful for high-power rather than high-energy applications.<sup>21</sup> In the case of alloying-type metal oxide anodes, such as SnO<sub>2</sub>, GeO<sub>2</sub>, ZnO,<sup>22-24</sup> continuous aggregation of building blocks during (de)lithiation leads to rapid capacity degradation.<sup>22,25</sup> This issue is avoided by using transition metal (TM) oxides, since TMs do not alloy with lithium. In conversion-type TM oxide anodes, the Li-storage mechanism involves a reversible multielectron transfer reaction. Li reacts with the TM oxide leading to the formation of a metallic TM nanonetwork and Li<sub>2</sub>O nanoclusters, whose decomposition accompanies the re-oxidation of metallic TM nanoparticles.<sup>26-29</sup> In recent years, TM oxides have attracted much academic and industrial interest as anode-materials for next generation LIBs due to their high theoretical capacity (600–1200 mAh g<sup>-1</sup>,<sup>25,27,30-37</sup>) compared to traditional graphite. However, they suffer from the low electrical conductivity, mechanical degradation and pulverization due to the

<sup>z</sup>E-mail: [marco.giorgetti@unibo.it](mailto:marco.giorgetti@unibo.it); [nicola.pinna@hu-berlin.de](mailto:nicola.pinna@hu-berlin.de); [saveria.santangelo@unirc.it](mailto:saveria.santangelo@unirc.it)

large volume changes during cycling, and excessive generation of SEI on the electrode surface owing to the electrolyte decomposition,<sup>33,37–39</sup> which represent the chief obstacles to be overcome for the broad application of TM oxide-based anodes for LIBs.<sup>39</sup>

Various strategies are commonly adopted to cope with the drawbacks responsible for the unsatisfactory performance and short life of the battery. The incorporation of dopants into the lattice or of the active material nanoparticles (NPs) into a carbonaceous matrix is frequently reported to improve the electrical transport properties,<sup>40–43</sup> whereas nano-sizing of the active material, besides increasing the effective lithium-ion diffusion transport rate, allows for the accommodation of strains associated with lithium insertion, thus improving rate capability (RC) and prolonging the battery cycle life.<sup>25,44–46</sup> The control of the geometric configuration enables the achievement of stable interfaces between the electrolyte and active material, resulting in SEI formation confined on its outer surface.<sup>37</sup> In this scenery, a deep understanding of the charge storage mechanism and related material structural changes is of pivotal importance to enhance the battery performance and life.

Recently, high-entropy materials,<sup>47–53</sup> which take advantage from the cooperative mixing of their multiple metallic components and the synergistic interaction between them, resulting in the so-called “cocktail effect”<sup>54,55</sup> have gathered much attention due to their unique properties for a wide range of applications.<sup>52,56</sup> Their high configurational entropy is thought to be responsible for stabilizing the microstructure.<sup>50</sup> Thanks to the integration of multiple redox couples, modulating of the electron reaction pathway,<sup>57</sup> high-entropy oxides show great potential for application in rechargeable alkali metal-ion batteries.<sup>58–66</sup> In particular, the superior properties in lithium-storage of  $(\text{Mg}_{0.2}\text{Co}_{0.2}\text{Ni}_{0.2}\text{Cu}_{0.2}\text{Zn}_{0.2})\text{O}$ , the first single-phase rock-salt-type high-entropy oxide (RHEO) synthesized in 2015,<sup>50</sup> have been reported by many research groups.<sup>61,65–71</sup> Compared to RHEOs, spinel-structured high-entropy oxides (SHEOs) have greater potential as anode materials because their structure can provide three-dimensional (3D) pathways for ionic diffusion,<sup>72</sup> resulting in higher  $\text{Li}^+$ -storage capacity.<sup>73</sup> Several SHEOs have been evaluated as anode materials for LIBs.<sup>42,74–81</sup> Their electrochemical properties strongly vary with the selected metal combination, and method and conditions of preparation, as well. Just to give a brief overview,  $(\text{Cr},\text{Mn},\text{Fe},\text{Co},\text{Ni})$  SHEO nanoparticles synthesized via a surfactant-assisted hydrothermal method, at  $20 \text{ mA g}^{-1}$ , exhibit a reversible charge/discharge capacity of  $1235 \text{ mAh g}^{-1}$ ,<sup>74</sup> whereas  $(\text{Cr},\text{Mn},\text{Fe},\text{Co},\text{Ni})$  SHEO produced by solid state reaction (SSR) delivers  $402 \text{ mAh g}^{-1}$  capacity after 300 cycles at  $0.5 \text{ A g}^{-1}$ .<sup>75</sup>  $(\text{Ti},\text{Mn},\text{Fe},\text{Co},\text{Ni})$  SHEO prepared by solid state sintering shows a reversible capacity of  $560 \text{ mAh g}^{-1}$  with 100% capacity retention after 100 cycles at  $0.1 \text{ A g}^{-1}$ .<sup>76</sup>  $(\text{Fe},\text{Ni},\text{Cr},\text{Mn},\text{Mg},\text{Al})$  SHEO synthesized by modified solution combustion method followed by ball milling shows a stable capacity of  $657 \text{ mAh g}^{-1}$  after 200 cycles at  $0.2 \text{ A g}^{-1}$ .<sup>82</sup> Oxygen-deficient  $(\text{Cr},\text{Mn},\text{Fe},\text{Co},\text{Zn})$  and  $(\text{V},\text{Mn},\text{Fe},\text{Co},\text{Zn})$  SHEOs produced via ball milling are able to deliver  $828.6$  and  $\approx 500 \text{ mAh g}^{-1}$  after 2000 cycles at  $2.0$  and  $3.0 \text{ A g}^{-1}$ , respectively.<sup>72,80</sup> Anodes based on electrospun  $(\text{Cr},\text{Mn},\text{Fe},\text{Co},\text{Zn})$  SHEO nanofibers (NFs) exhibit greater stability and higher reversible capacity than those prepared with  $(\text{Cr},\text{Mn},\text{Fe},\text{Co},\text{Zn})$  SHEO nanoparticles (NPs) produced by conventional sol-gel method.<sup>42</sup> RC and cycling stability of  $(\text{Cr},\text{Mn},\text{Fe},\text{Ni},\text{Cu})$  SHEOs prepared via hydrothermal method strongly depend on calcination temperature.<sup>83</sup> The good electrochemical performance of SHEO-based anodes is attributed to various factors, such as entropy stabilization effects that maintain the crystalline oxide framework during the lithiation and promote the recovery of the spinel phase during de-lithiation,<sup>74</sup> occurrence of amorphization process during the initial discharging,<sup>75</sup> balanced crystallinity and particle size associated with the high-entropy stabilization,<sup>83</sup> and formation of lithiated phases that help to stabilize the spinel structure.<sup>76</sup>

Very recently, electrospun  $(\text{Mn},\text{Fe},\text{Co},\text{Ni},\text{Zn})$  SHEO NFs with highly oxygen-deficient surface have been prepared under low environmental-impact calcination conditions ( $700 \text{ }^\circ\text{C}$  for only 30 min)<sup>81</sup> to both limit sintering effects on the size of the oxide NPs forming the NFs, and improve the electrode performance.<sup>70,80</sup> Their evaluation as an anode material in LIBs has shown an initial discharge capacity of  $1283.6 \text{ mAh g}^{-1}$  (at  $20 \text{ mA g}^{-1}$ ), which is among the highest values ever reported for SHEO-based anodes.<sup>81</sup> Although the anode based on these NFs suffers from an important initial decay in capacity due to extensive and irreversible structural changes, as typical of conversion anode-materials,<sup>84</sup> contrary to expectations,<sup>85</sup> after 550 cycles at  $0.5 \text{ A g}^{-1}$ , it still delivers a capacity of  $155 \text{ mAh g}^{-1}$ ,<sup>81</sup> higher than common intercalation-anodes based on commercial graphite powders ( $125 \text{ mAh g}^{-1}$  after 300 cycles at  $0.5 \text{ A g}^{-1}$ <sup>86</sup>), which suggests long-term structural stability of the oxide lattice. The investigation of the SHEO NF properties and mechanism of  $\text{Li}^+$  storage through a combination of analytical techniques including ex situ synchrotron X-ray absorption spectroscopy (XAS)<sup>81</sup> has evidenced that the capacity fading in the first cycles is associated with the partial irreversibility of the lithiation process, which occurs through incomplete conversion reactions and early intercalation, accompanied by a spinel to rock-salt phase transition, as in other spinel-structured TM oxides.<sup>83,84</sup>

Electrospinning, a scalable and cost-effective technique,<sup>87–89</sup> allows producing single-phase high-entropy oxides with different structures and related composites.<sup>42,70,71,90–92</sup> The metal loading in the spinnable precursor solution heavily affects both the diameter of the NFs and the size of the NPs that compose them.<sup>93,94</sup> The post-spinning calcination conditions (temperature and duration) strongly influence not only the morphology and crystallinity of the NFs,<sup>83,95,96</sup> but also the concentration of surface oxygen vacancies and defects,<sup>42,92,95,97</sup> the degree of spinel inversion and the distribution of cations in the SHEO lattice.<sup>92,96,97</sup>

In this work, electrospun  $(\text{Mn},\text{Fe},\text{Co},\text{Ni},\text{Zn})$  SHEO NFs to be used as anode active materials in LIBs are produced via the procedure utilized in a previous work<sup>81</sup> by varying the metal load ( $19.23$  or  $38.46 \text{ wt}\%$  relative to the polymer) in the precursor solution, and temperature and duration of the calcination process ( $0.5 \text{ h}$  at  $700 \text{ }^\circ\text{C}$ , or  $2 \text{ h}$  at  $700 \text{ }^\circ\text{C}$  followed by  $2 \text{ h}$  at  $900 \text{ }^\circ\text{C}$ ), as schematically depicted in Fig. S1. The rationale is to improve the NF electrochemical performance by (i) reducing the impact of mechanical stress associated with volume expansion and contraction during cycling through the integration of multiple redox couples,<sup>57,72</sup> (ii) obtaining a stable SEI through a uniform morphology and a narrow particle size range,<sup>7</sup> and (iii) forming a well-crystallized and stable oxide structure, capable of accommodating the structural changes associated to cation migration induced by the  $\text{Li}$ -ion insertion in the vacant lattice sites.<sup>32,81,98</sup>

The results of the electrochemical tests and of the thorough characterization of the active material by a combination of analytical techniques are comparatively discussed to investigate to what extent the effects produced by the variation of metal load in the precursor solution and of the calcination process conditions on the morphology, microstructure, phase, crystallinity, inversion degree, cation distribution and surface composition of the pristine SHEO NFs reflect on their electrochemical performance. Besides, the changes introduced by the variation of the preparation conditions of the active material in the mechanism of  $\text{Li}^+$  storage are investigated by carrying out ex situ X-ray diffraction, micro-Raman spectroscopy, electron microscopy and synchrotron XAS<sup>99</sup> measurements. Such comparative investigation reveals that NFs calcined under more severe conditions exhibit far superior performance as anode materials compared to the others.<sup>81</sup> As shown below, after optimization, they have better LTS than other HEO-based conversion anodes and a RC equal to that of the best HEO anodes.

## Experimental

### Synthesis of the high-entropy (Mn,Fe,Co,Ni,Zn) oxide NFs.—

The high-entropy (Mn,Fe,Co,Ni,Zn) oxide NFs were prepared by electrospinning, following the procedure described in detail in a previous paper.<sup>42,81</sup> Polyacrylonitrile (PAN, 150000 g mol<sup>-1</sup>, 99.9%) and N,N-dimethylformamide (DMF, anhydrous, 99.8%) were used for the preparation of the precursor polymer/solvent solution. Manganese(II) acetate tetrahydrate (99%), iron (II) acetate (95%), cobalt (II) acetate tetrahydrate (99%), nickel (II) acetate tetrahydrate (98%) and zinc (II) acetate dihydrate (98%) acted as Mn, Fe, Co, Ni and Zn sources, respectively. Stoichiometric amounts of these salts were dissolved in the PAN/DMF solution to obtain the desired total load of metals (38.46 or 19.23 wt% relative to PAN).

To remove their organic components the as-spun polyacrylonitrile/(Mn,Fe,Co,Ni,Zn)-acetates NFs were calcined in air under conditions reported in Fig. S1. In the following, SHEO NFs produced under milder conditions (700 °C for 0.5 h) are coded as mcHEO, whereas those calcined for longer time at higher temperature (700 °C for 2 h and 900 °C for 2 h) are referred as HEO NFs. Metal load (ML) in the precursor solution to prepare mcHEO and HEO NFs is 38.46 wt% (relative to the polymer); a subscript LL is added to the code of the NFs obtained by spinning a precursor solution with 19.23 wt% ML and subsequent calcination under the same conditions as mcHEO and HEO NFs (Fig. S1).

**Characterization.**—The Li-ion storage properties of the high-entropy (Mn,Fe,Co,Ni,Zn) oxide NFs were investigated by recording galvanostatic charge/discharge (GCD) and cyclic voltammetry (CV) curves. Morphology, texture, microstructure, crystalline phase and surface composition of the pristine NFs were investigated by carrying out scanning electron microscopy (SEM), transmission electron microscopy (TEM), X-ray diffraction (XRD), micro-Raman spectroscopy (MRS) and X-ray photoelectron spectroscopy (XPS) analyses. To get a deeper insight into the charge storage mechanism and associated structural, morphological and compositional changes, ex situ synchrotron XAS, XRD, MRS, TEM and STEM/EDX analyses were conducted.

**Electrochemical properties.**—To investigate the electrode performance of samples, CR2032-type coin cells were assembled in an Ar-filled glovebox. The as-prepared NFs were homogeneously mixed by using mortar and pestle with 20 wt% conductive carbon black (Super P, Timcal), 10 wt% poly(vinylidene fluoride) binder (PVDF, Alfa Aesar) and N-methyl-2-pyrrolidone (NMP, Sigma-Aldrich). The obtained slurry was uniformly coated onto Cu foil with a doctor blade apparatus. The electrodes were cut in a diameter of 12 mm with the active material mass load of 1.0–1.5 mg cm<sup>-2</sup>, which were dried for 10 h at 90 °C under vacuum. Lithium metal foil was used as negative electrodes. 1 mol l<sup>-1</sup> LiPF<sub>6</sub> solution in ethylene carbonate (EC)/diethyl carbonate (DEC)/dimethyl carbonate (DMC) (1:1:1 volume ratio) was used as the electrolyte. One layer of porous glass fiber (Whatman) was used as separator.

All coin cells were cycled using a CT2001A battery testing system (Landt Instruments) at room temperature within the voltage range of 0.01–3.0 V (vs Li<sup>+</sup>/Li). Bio-Logic VMP3 multichannel potentiostat/galvanostat was conducted to record CV results.

**Morphology, texture, microstructure, crystalline phase and surface composition of the NFs.**—A Phenom Pro-X scanning electron microscope, operating at 15 kV, was used to obtain SEM images. Additionally, a FEI Talos F200S scanning/transmission electron microscope, operating at 200 kV, was used for TEM, HRTEM (high-resolution TEM), HAADF-STEM (high-angle annular dark-field scanning TEM), ED (electron diffraction), and EDX elemental mappings. The NF inner morphology was investigated through projection analysis of STEM-EDX maps. Geometrical phase analysis (GPA) of lattice fringes in HRTEM images provided

structural information about the primary particles. Further information on the projection analysis of EDX elemental maps and GPA analysis can be found in Ref. 61 and the Supplemental Material (SM).

XRD analysis was carried out using a Bruker D2 diffractometer with Ni  $\beta$ -filtered Cu-K $\alpha$  radiation ( $\lambda = 0.1541$  nm). Selected diffractograms were analyzed by the Rietveld method using Maud 2.992 software. Crystallite size and microstrain were modeled employing an isotropic size-strain model with Delft line broadening.<sup>100</sup> Raman scattering measurements were performed using a NTEGRA—Spectra SPM NT-MDT confocal microscope coupled to a solid-state laser operating at 2.33 eV (532 nm), ensuring a laser power of 250  $\mu$ W at the sample surface to prevent local heating. The scattered light was collected by a 100X Mitutoyo objective, dispersed by an 1800 lines mm<sup>-1</sup> grating, and detected by a cooled ANDOR iDus CCD Camera. To assess spatial homogeneity, spectra were recorded from various random positions on each specimen, and their average provided a reliable representation of the entire sample. The averaged spectra were fitted to Gaussian bands, with the amplitude ratio reflecting the relative intensity of each mode due to variations in sample preparation conditions.

XPS studies were performed using an EnviroESCA spectrometer (Specs), equipped with an AlK $\alpha$  X-ray source ( $h\nu = 1486.6$  eV). Spectra were acquired at ca. 10<sup>-6</sup> mbar. High-resolution spectra were collected using a pass energy of 50 eV, integrating for 0.1 sec·step<sup>-1</sup>, and acquiring every 0.1 eV·step<sup>-1</sup>. Spectra were shifted in binding energy (BE) in order to correct the experimental error resulting from the charge accumulation phenomenon. To do this, a BE value of 284.8 eV was imposed to adventitious carbon.<sup>101</sup> XPS curves were decomposed with the Keystone software (Specs) and using a Shirley-type background.<sup>102</sup> Quantification parameters were provided by Specs.

**XAS analysis.**—XAS experiments were performed on XAFS beamline<sup>103</sup> at Elettra Synchrotron Trieste (Italy). The storage ring was operating in the top-up mode at 2.0 GeV, with a typical current of 300 mA. The monochromatization of the white beam was achieved by a fixed exit monochromator, equipped with a pair of Si (111) crystals. Data were recorded at Fe, Mn, Co, Ni and Zn K-edges in transmission mode. The electrodes studied ex situ in this experiment were detached from the Cu foil and were fixed on the sample holder with Kapton tape. Iron, manganese, cobalt, nickel and zinc foils were used as internal references for the energy calibration in each scan. This allowed a continuous monitoring of the energy during consecutive scans. The white beam was monochromatized using a fixed exit monochromator equipped with a pair of Si (111) crystals. Spectra were collected with 1 s per point acquisition time from 6244 to 7100 eV for Mn, from 6817 to 7672 eV for Fe, from 7514 to 8302 eV for Co, from 8138 to 8978 eV for Ni, and from 9467 to 10634 eV for Zn K-edges. A constant k-step of nm<sup>-1</sup> was utilized. XAS spectra were calibrated and analyzed using the Athena program.<sup>104</sup>

## Results and Discussion

**Electrochemical behavior in LIBs.**—The electrochemical behavior of (Mn,Fe,Co,Ni,Zn) SHEO NFs was studied in half cells with Li anodes. The lithium-driven redox reactions and structural transformation occurring during discharge/charge process were studied by CV. The results obtained in the 0.01–3.0 V potential range at a scan rate of 0.1 mV s<sup>-1</sup> are displayed in Figs. 1a–1c. Two peaks at 0.6–0.7 and 0.9–1.1 V are detected in the first cathodic scan (lithiation) of mcHEO<sub>LL</sub> (Fig. 1a), HEO (Fig. 1b) and HEO<sub>LL</sub> NFs (Fig. 1c). They originate from the formation of SEI layer on the material surface due to the electrolyte decomposition<sup>66,70,74</sup> and from the reduction of electrochemically active cations and the formation of Li<sub>2</sub>O<sup>39,61,69,78</sup> and irreversible change of crystal structure.<sup>78</sup> The peaks detected at ca. 1.7 and 2.1 V in the subsequent anodic scan (de-lithiation) are due to the re-oxidation process of the redox-active species and the decomposition of Li<sub>2</sub>O.<sup>74</sup> In the



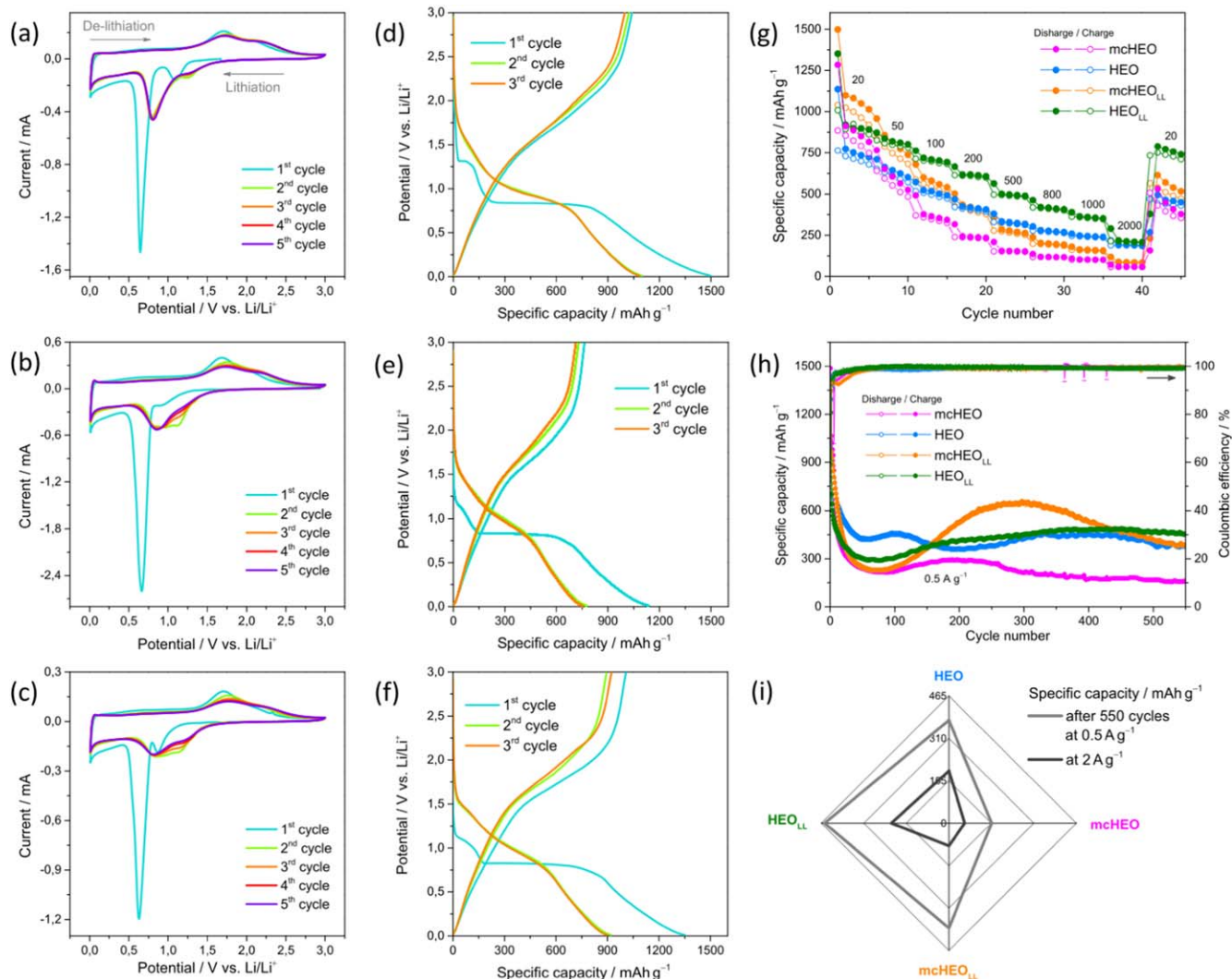


**Figure 1.** Electrochemical performance of the electrospun high-entropy (Mn,Fe,Co,Ni,Zn) spinel oxides in the Li-ion half cells. (a)–(c) CV curves recorded at  $0.1 \text{ mV s}^{-1}$  scanning rate and (d)–(f) galvanostatic charge–discharge curves measured at  $20 \text{ mA g}^{-1}$ ; the shown data refer to samples (a,d) mcHEO<sub>LL</sub>, (b), (e) HEO and (c,f) HEO<sub>LL</sub>. (g) RC at different current densities (expressed in  $\text{mA g}^{-1}$ ), (h) LTS at a current density of  $500 \text{ mA g}^{-1}$  (the results relative to mcHEO are also reported for comparison) and (i) specific capacity measured in RC tests at  $2.0 \text{ A g}^{-1}$  and in LTS tests after 550 cycles at  $0.5 \text{ A g}^{-1}$ .

following four cycles, both the cathodic and the anodic peaks shift towards slightly higher potentials, as previously observed in the case of mcHEO NFs.<sup>81</sup> In the CV curves of mcHEO<sub>LL</sub> (Fig. 1a), all peaks appear well overlapping, evidencing the good reversibility of lithiation/de-lithiation in these NFs. Oppositely, some little change is still observed in the higher-potential cathodic peak of HEO (Fig. 1b) and HEO<sub>LL</sub> NFs (Fig. 1c).

The first three GCD curves of mcHEO<sub>LL</sub>, HEO and HEO<sub>LL</sub> NFs are shown in Figs. 1d–1f, respectively. The initial discharge and charge capacities of SHEO NFs are reported in Table S2. As a general result, regardless of the calcination conditions, higher discharge/charge capacities pertain to NFs produced from spinnable solutions with lower ML (mcHEO<sub>LL</sub> and HEO<sub>LL</sub>). However, the preparation conditions of SHEO NFs seem not to greatly affect the corresponding initial Coulombic efficiencies (ICEs), which are comparable to each other, slightly higher in the case of NFs calcined under milder conditions (69% against 67%, values that both exceed the ICE reported for (Cr,Mn,Fe,Co,Ni) SHEO prepared by SSR at  $900 \text{ }^\circ\text{C}$ <sup>75</sup>). The decomposition of the electrolyte to form the SEI layer and the occurrence of irreversible structural rearrangements are responsible for the capacity loss of the first cycle.<sup>69,75,78,81</sup> Upon calcination at  $700 \text{ }^\circ\text{C}$  for 0.5 h, higher 2nd discharge capacity values

(and 2nd/1st discharge capacity ratio) are obtained, regardless of the ML (Table S2).

The RC of SHEO NFs was evaluated at current densities from 20 to  $2000 \text{ mA g}^{-1}$  (Fig. 1g). At  $20 \text{ mA g}^{-1}$ , the lithiation capacities increase in the order HEO ( $773 \text{ mAh g}^{-1}$ ) < mcHEO ( $912 \text{ mAh g}^{-1}$ <sup>81</sup>) < HEO<sub>LL</sub> ( $920 \text{ mAh g}^{-1}$ ) < mcHEO<sub>LL</sub> ( $1098 \text{ mAh g}^{-1}$ ), indicating that higher capacity values are obtained by the use of precursor solutions with lower ML. However, with increasing rate, the capacities of NFs calcined under milder conditions reduce more rapidly than those of HEO and HEO<sub>LL</sub> NFs. At  $2000 \text{ mA g}^{-1}$  (Fig. 1i), the lithiation capacities vary in the order mcHEO ( $58 \text{ mAh g}^{-1}$ ) < mcHEO<sub>LL</sub> ( $83 \text{ mAh g}^{-1}$ <sup>81</sup>) < HEO ( $191 \text{ mAh g}^{-1}$ ) < HEO<sub>LL</sub> ( $210 \text{ mAh g}^{-1}$ ), respectively. This finding suggests that, regardless of the ML in the spinnable solution, SHEO NFs calcined at higher temperature exhibit superior RCs (Table S2). When the current density is set back to  $20 \text{ mA g}^{-1}$ , capacities of 495, 539, 615 and  $788 \text{ mAh g}^{-1}$  are recovered for HEO, mcHEO, mcHEO<sub>LL</sub> and HEO<sub>LL</sub> NFs, respectively. The percentages of recovered capacity (64, 59, 56 and 86%, respectively) suggests that, at any ML in the spinnable solution, a better-crystallized SHEO lattice is beneficial also to the capacity recovery (Table S2). At  $2000 \text{ mA g}^{-1}$ , the capacity delivered by HEO<sub>LL</sub> NFs exceeds those reported, at the same rate, for (Cr,Mn,Fe,Co,Ni) SHEO prepared by SSR

at 900 °C (180 mAh g<sup>-1</sup><sup>75</sup>) and electrospun (Cr,Mn,Fe,Co,Zn) SHEO NFs calcined at 900 °C (28 mAh g<sup>-1</sup>);<sup>42</sup> it is comparable to those of (Cr, Mn,Fe,Ni,Cu) SHEO synthesized via hydrothermal method followed by calcination at 1000 °C (220 mAh g<sup>-1</sup>),<sup>83</sup> and electrospun (Mg,Co,Ni,Cu, Zn) RHEO NFs (207 mAh g<sup>-1</sup>).<sup>71</sup>

LTS is a factor of pivotal importance for the practical use of LIBs. Therefore, developing electrode materials able to maintain their integrity over many discharge/charge cycles is a challenging issue. Figure 1h displays the results of evaluation of the cycling stability of SHEO NFs at a current density of 500 mA g<sup>-1</sup>. For all NFs, the specific capacity exhibits a non-monotonic trend. After the initial rapid decrease, probably originating from the lithium-driven irreversible structure transformation,<sup>78</sup> it smoothly increases reaching a constant value only in the case of HEO<sub>LL</sub> NFs; differently, some fluctuations are observed in the case of mcHEO and HEO NFs, and more markedly in the case of mcHEO<sub>LL</sub> NFs. Such behavior, frequently reported for both low- and high-entropy TM oxides,<sup>61,83,105</sup> is attributed to a possible activation process in the electrode,<sup>106</sup> due to the gradual electrolyte penetration<sup>77</sup> and increase in interfaces.<sup>107</sup> The capacity retained after 550 cycles at 0.5 A g<sup>-1</sup> (Fig. 1i) varies in the order mcHEO (156 mAh g<sup>-1</sup><sup>81</sup>) < HEO (376 mAh g<sup>-1</sup>) < mcHEO<sub>LL</sub> (383 mAh g<sup>-1</sup>) < HEO<sub>LL</sub> (453 mAh g<sup>-1</sup>). All these values exceed that reported for conventional intercalation-anodes based on commercial graphite powders cycled at the same rate (125 mAh g<sup>-1</sup> after 300 cycles<sup>86</sup>), and compare well with those reported for conversion-anodes based on high-entropy oxides. At 0.5 A g<sup>-1</sup>, electrospun (Cr,Mn,Fe,Ni,Zn) SHEO and (Mg,Co,Ni,Cu,Zn) RHEO NFs calcined at 900 °C, (Cr,Mn,Fe,Co,Ni) SHEO obtained by SSR reaction at 1000 °C and (Cr,Mn,Fe,Ni,Zn) SHEO prepared via ball-milling and 12 h calcination at 900 °C retain 265 mAh g<sup>-1</sup> after 400 cycles,<sup>42</sup> 390 mAh g<sup>-1</sup> after 300 cycles,<sup>71</sup> and 402 mAh g<sup>-1</sup> after 300 cycles<sup>75</sup> and 387 mAh g<sup>-1</sup> after 185 cycles,<sup>79</sup> respectively. At lower rate (0.2 A g<sup>-1</sup>), the rate of decrease in capacity of HEO<sub>LL</sub> NFs is halved (-2 mAh g<sup>-1</sup> cycle<sup>-1</sup> against -4 mAh g<sup>-1</sup> cycle<sup>-1</sup> at 0.5 A g<sup>-1</sup>) and the anode still retains 612 mAh g<sup>-1</sup> after 100 cycles (Fig. S2), a capacity value comparable to that reported for (Mg,Co,Ni, Cu,Zn) RHEO prepared by nebulized spray pyrolysis method.<sup>61</sup>

Summarizing, the HEO<sub>LL</sub>-based anode is superior to the others both in terms of (i) high current density capability and capacity recovery; and (ii) LTS. In the following, the existence of a correlation between electrochemical performance and morphological and microstructural properties of the active material is investigated.

**Physicochemical properties of the pristine NFs.**—In order to investigate the relationship between the electrochemical performance of SHEO NF-based anodes and the physicochemical properties of pristine active materials, SEM, TEM, XRD, MRS and XPS analyses were carried out.

**Morphology and microstructure.**—Figures 2a–2h, 2m, S3 and S4 summarise the results of the morphological analyses. SEM images (Fig. S3) demonstrate that micrometer-long NFs are formed under all preparation conditions. Their diameters ( $d_{NF}$ ) vary in broad ranges (Table S3), with the distributions of the fibers derived from solution with lower ML centered on smaller values (Fig. 2m), as expected.<sup>93,94</sup>

TEM analysis (Figs. 2a–2h and S4) reveals that, although all fibers consist of interconnected crystalline grains having polyhedral shapes, their morphology is different. HEO<sub>LL</sub> NFs have a segmented, branched structure, similar to that previously observed in the case of (Mg,Co,Ni,Cu,Zn) RHEO NFs, exhibiting good performance as anode material in LIBs.<sup>71</sup> In mcHEO, mcHEO<sub>LL</sub> and HEO NFs, the space-confined oxide grains, formed because of the expansion and contraction experienced by polymer and embedded TM acetates, respectively,<sup>108,109</sup> during the degradation of organic components of the pristine fibers upon calcination, are attached to each other to form a porous, three-dimensional (3D), straight, filamentous structure, as peculiar to electrospun oxides.<sup>41,95,110–113</sup>

Such an architecture, capable of accommodating volume changes and affording short paths for Li-ions, is considered beneficial for the electrochemical performance as it ensures suitable conductivity and mechanical strength over extended electrode cycling.<sup>37,98</sup>

The size of SHEO grains ( $d_G$ ) depends on both the ML and calcination conditions and increases in the order mcHEO < mcHEO<sub>LL</sub> < HEO < HEO<sub>LL</sub>. This finding proves that heavier sintering effects occur at higher calcination temperature ( $T_C$ ), as expected,<sup>114,115</sup> and, at a given temperature, with decreasing ML. Surprisingly, the anode prepared with the fibers (HEO<sub>LL</sub>) constituted by grains with the largest average size outperforms the remaining ones in the LTS tests (Figs. 1h, 1i), contrary to the common assumption that nano-sizing improves battery performance in terms of cyclability. This result agrees with other literature reports<sup>32,98,105</sup> and with the existence of an optimal particle size to enhance battery performance, as demonstrated for ZnMn<sub>2</sub>O<sub>4</sub>.<sup>116</sup>

Figures 2i, 2j displays the results of elemental mapping via STEM/EDX analysis on HEO NFs, as a representative case. The results of projection analysis of the elemental maps (Fig. S5a), illustrated in detail in SM and in a previous paper,<sup>97</sup> prove that, regardless of the preparation conditions, the dispersion of Mn, Fe, Co, Ni, Zn and O is spatially uniform and the TM combination is nearly-equimolar in all NFs. In addition, the fit of oxygen longitudinal projection to model profiles (Fig. S5b) reveals that, except for HEO<sub>LL</sub>, the NFs have a narrow inner channel; its size increases from 20% of the fiber width in mcHEO, to 30% in HEO, in agreement with previous reports on electrospun SHEOs based on different TM combinations<sup>96</sup> and low-entropy oxide NFs, as well.<sup>95</sup> The large temperature gradient along the radial direction experienced by the precursor polymer/TM-acetate NFs during calcination<sup>117</sup> due to the rapid rise in temperature (10 °C min<sup>-1</sup>) and the sintering effects,<sup>95</sup> which favor the development of larger grains at the expense of smaller ones, with a decrease in the specific surface,<sup>118</sup> are responsible for the above described evolution of fiber microstructure and may also affect the electrochemical performance of the fibers.<sup>119</sup>

**Oxide phase, crystallinity and inversion degree of the pristine NFs.**—Figure 2k shows the XRD patterns of the SHEO NFs. All reflections detected in the diffractograms of the NFs calcined under milder conditions can be indexed to the spinel structure (JCPDS no. 22–1084).<sup>8,74,75,120–123</sup> Rietveld refinements from XRD data (Figs. S6a, S6b) confirm the formation of pure single-phase spinel without any secondary phase(s). On the contrary, in the diffractograms of HEO and HEO<sub>LL</sub> NFs, three weak additional peaks are detected, which can be ascribed to the segregation of a small part of the TMs into a rock-salt secondary phase (JCPDS no. 47–1049).<sup>63,65,71,103,120,124–126</sup> The origin for its formation in samples calcined at higher temperature (700 °C/2 h, followed by 900 °C/2 h) is not clear. Nonetheless, the presence of a rock-salt component in the oxide has no impact on its electrochemical performance because, as shown in the following, a progressive spinel to rock-salt phase transformation occurs during the first discharge/charge cycles, in agreement with other literature reports on spinel-structured anode materials. Rietveld refinements (Figs. S6c, S6d) indicate that the relative amount of this phase is 8–10 w%, in agreement with previous findings.<sup>42</sup> The average size of SHEO crystallites ( $d_{SHEO}$ , shown in Fig. 2n), which gives a measure of the effectiveness of the crystallization process, increases in the order mcHEO (59 nm<sup>81</sup>) < mcHEO<sub>LL</sub> (68 nm) < HEO (95 nm) < HEO<sub>LL</sub> (130 nm). Thus, larger domains with spinel lattice-ordering are obtained for a lower ML under given heating conditions, and upon calcination at higher  $T_C$  for a given ML. The comparable values of  $d_{SHEO}$  and  $d_G$  indicate that the fibers are mainly formed by interconnected single crystals. In addition, the increase of  $d_{SHEO}$  and  $d_G$  in the same order as the capacity value measured in the RC tests at 2.0 A g<sup>-1</sup> (Fig. 1g and Table S2) represents a further confirmation that larger and better-crystallized grains forming the NFs are beneficial for cyclability of the battery, in agreements with the existence of a capacity/particle-size correlation.<sup>32,98,105</sup>

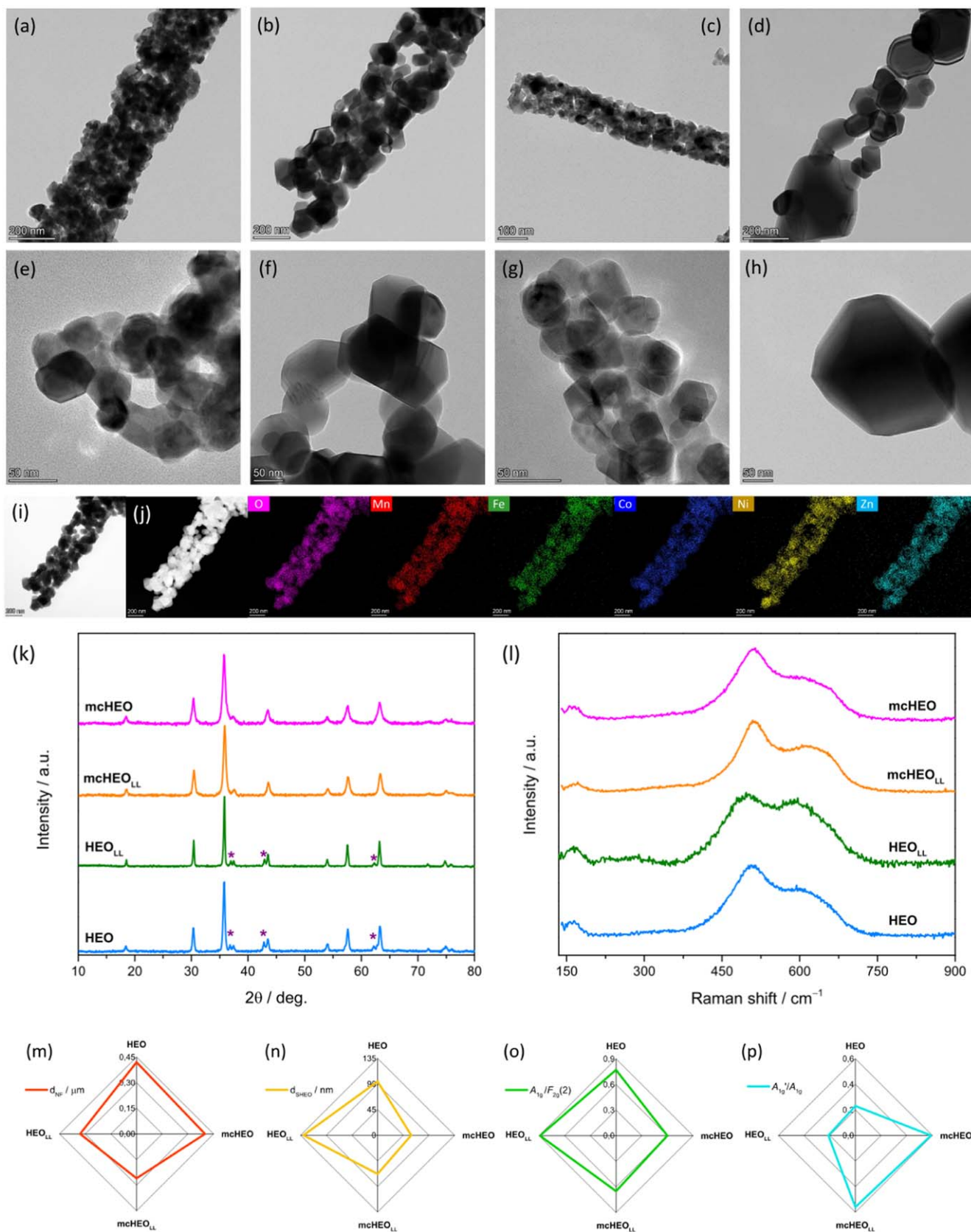


**Figure 2.** Results of the (a)–(j) (S)TEM, (k) XRD and (l) micro-Raman analyses. (a)–(d) TEM and (e)–(h) HRTEM images of samples (a,e) mcHEO, (b, f) HEO, (c, g) mcHEO<sub>LL</sub> and (d, h) HEO<sub>LL</sub>. (i) BF-STEM, and (j) HAADF-STEM images of sample HEO, followed by STEM/EDX elemental maps. (k) XRD patterns (stars mark reflections from secondary rock-salt structured phase). (l) Micro-Raman spectra. (m)–(p) Main parameters inferred from (m) SEM, (n) XRD and (o), (p) MRS analyses.



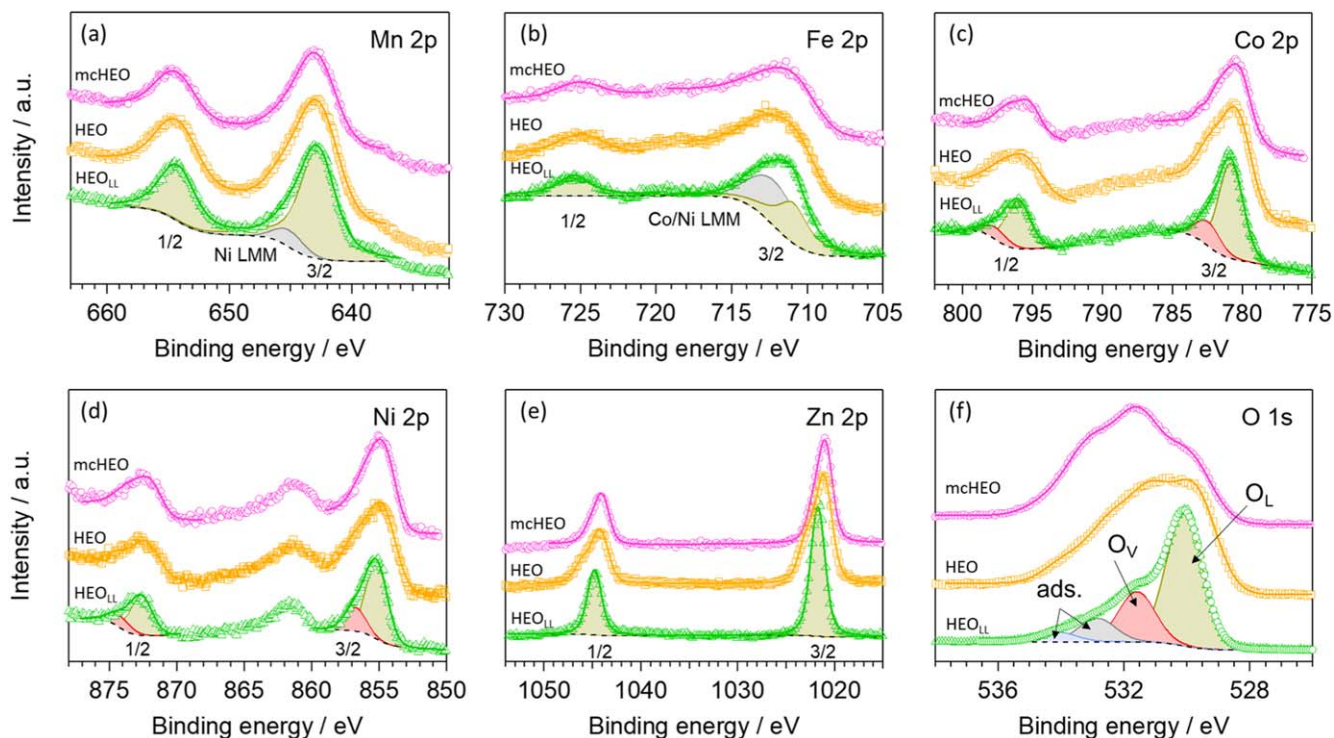


**Figure 3.** High resolution XPS spectra for the three analyzed samples in the regions of Mn 2p, Fe 2p, Co 2p, Ni 2p, Zn 2p and O 1s core levels.

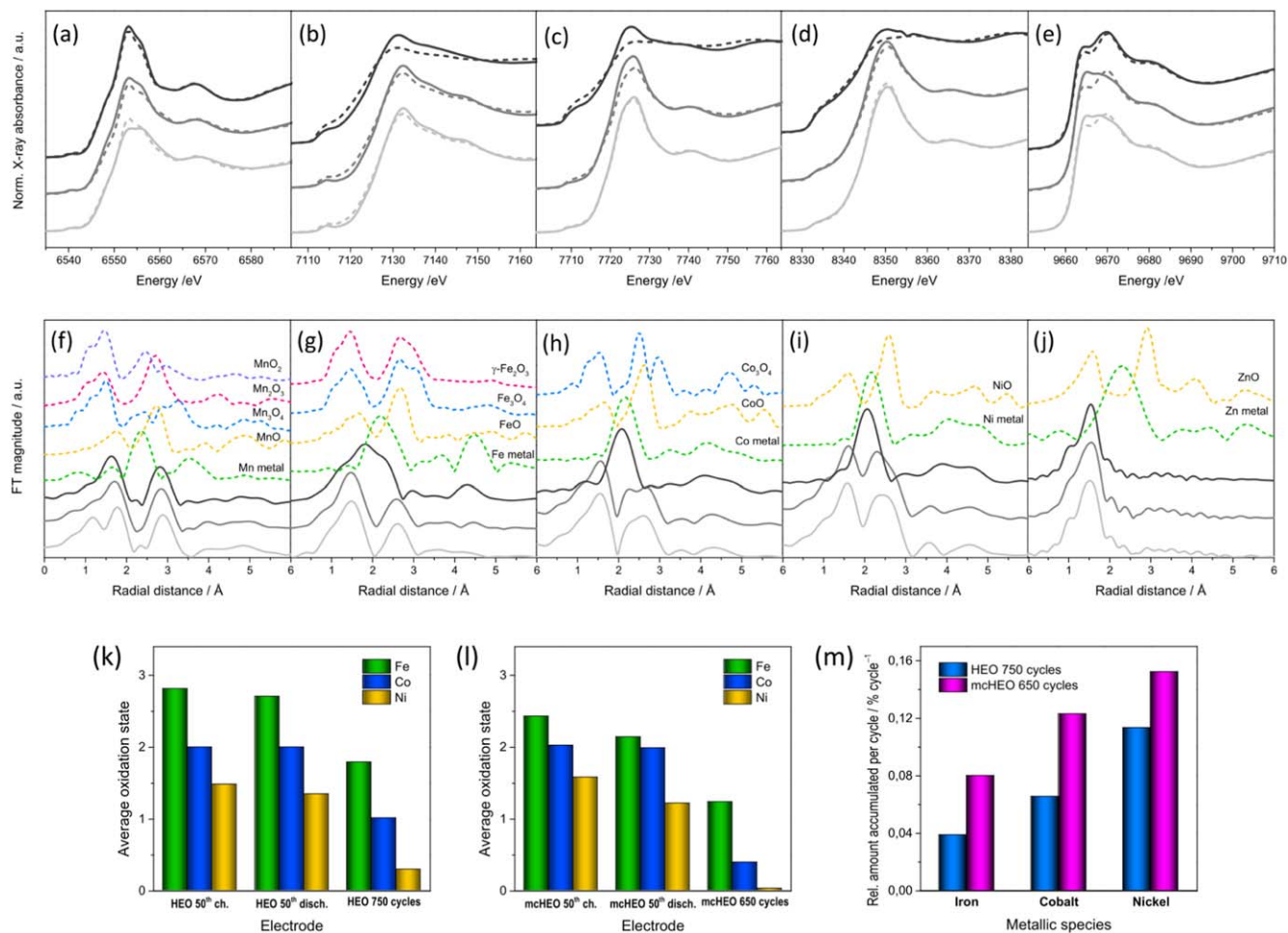
Figure 2l shows the micro-Raman spectra obtained by averaging the spectra recorded at several random locations on each specimen. As previously discussed in detail,<sup>42,96,97</sup> five Raman-active normal vibration modes ( $A_{1g} + E_g + 3F_{2g}$ ) are predicted for the spinel structure ( $Fd-3m$  space group),<sup>127–130</sup> their frequency positions and relative intensities strongly vary within the family of spinels.<sup>128,129,131,132</sup> The fit of the spectra to Gaussian bands (Figs. S6e–S6h) reveals that the intensity of  $A_{1g}$  mode, involving the vibration along the direction joining an oxygen atom to the tetrahedral  $M^{2+}$  cation,<sup>97</sup> increases relative to the most intense  $F_{2g}(2)$  asymmetric oxygen stretching mode,<sup>97</sup> with increasing  $T_C$  and, at a given  $T_C$ , with decreasing ML (Fig. 2o and Table S3), in agreement with the literature.<sup>133</sup> The  $A_{1g}/F_{2g}(2)$  intensity ratio linearly correlates with  $d_{SHEO}$ , the larger  $d_{SHEO}$ , the higher the  $A_{1g}/F_{2g}(2)$  intensity ratio. In addition to the normal phonon modes, inversion-induced modes<sup>120,129,134</sup> also contribute to the Raman intensity in all NFs ( $E_g'$  and  $A_{1g}'$  modes in Figs. S6e–S6h), in full agreement with both literature reports on SHEOs<sup>134</sup> and previous studies.<sup>42,92,96,97</sup> The inversion degree of the spinel lattice, as monitored by the  $A_{1g}'/A_{1g}$  intensity ratio (Fig. 2p and Table S3), decreases with increasing  $T_C$ , as expected.<sup>81</sup>

Figure S7 shows the equilibrium distribution and completely random distribution, as inferred from simple consideration of electronegativity and crystal-field octahedral stabilization energy,<sup>92,96,97</sup> for SHEOs based on an equimolar combination of Mn, Fe, Co, Ni and Zn cations (as in present NFs). The cation distributions in the NFs calcined at higher and lower  $T_C$  are expected to be closer to the former and the latter, respectively. Therefore, the linear increase of  $A_{1g}'/F_{2g}(2)$  Raman band intensity ratio with  $d_{SHEO}$  (Table S3) monitors the progressive increase in the occupation of the tetrahedral sites by  $M^{2+}$  cations that accompanies the increase in the oxide crystallinity, i.e. the evolution towards the equilibrium cation distribution (Fig. S7). An analogous consideration applies to the decrease in the inversion degree with  $T_C$ , as monitored by the  $A_{1g}'/A_{1g}$  intensity ratio (Fig. 2p).

**Surface composition of the pristine NFs.**—XPS survey spectra (Fig. S8) reveal the presence of Mn, Fe, Co, Ni, Zn, O and C (adventitious carbon) on the surface of the electrospun SHEO NFs. The elemental composition is not constant among the different materials (Table S4) and is strongly affected by the ML in the precursor solution and the conditions of the calcination process. The manganese concentration decreases in the order HEO<sub>LL</sub> > HEO > mcHEO, reaching values of 9.32, 7.08 and 5.58 at%, respectively. Iron is mostly present in HEO<sub>LL</sub> sample (2.47 at%), while in HEO and mcHEO NFs it accounts for ca. 1.5 at%. The cobalt content decreases in the order mcHEO > HEO<sub>LL</sub> > HEO (6.77, 4.45 and 3.90 at%, respectively). A similar concentration of nickel is detected for all NFs (i.e., ca. 4.5 at%). Zinc has a similar trend as manganese: 8.98, 8.09 and 6.34 at% for HEO<sub>LL</sub>, HEO and mcHEO NFs, respectively.

High-resolution XPS investigations allow inferring information on the oxidation states of the elements composing the surface of the investigated materials. It must be pointed out that the presence of several Auger lines belonging to the different TMs could limit the accuracy of data analysis in the overlapping spectral regions. In the Mn 2p spectral region (Fig. 3a), three peaks are observed at ca. 642.9, 654.3 and 645.8 eV. They are attributed to Mn 2p<sub>3/2</sub>, Mn 2p<sub>1/2</sub> and Ni LMM, respectively.<sup>135</sup> This is coherent with the presence of Mn(IV) surface species.<sup>136</sup> In the Fe 2p spectral region (Fig. 3b), the 2p<sub>3/2</sub> and 2p<sub>1/2</sub> spin-orbit components are detected at ca. 710.5 and 725.1 eV in HEO and mcHEO NFs. For HEO<sub>LL</sub> NFs, these peaks shift towards higher BE values by +0.4 eV, indicating a higher oxidation state for the Fe atoms. Overall, the detected BE values demonstrate the possible co-existence of species with oxidation states comprised between +2 and +3.<sup>92,97</sup> Four different peaks contribute to the intensity of the Co 2p signal (Fig. 3c): (i) the 2p<sub>3/2</sub> features of Co<sup>2+</sup> and Co<sup>3+</sup>, peaking at ca. 780.2 and 781.5, respectively,<sup>137,138</sup> (ii) the 2p<sub>1/2</sub> features of Co<sup>2+</sup> and Co<sup>3+</sup>, peaking at ca. 795.2 eV and 796.6 eV, respectively.<sup>132,133</sup> In the case of HEO<sub>LL</sub> NFs, peaks are shifted by +0.8 or 0.9 eV, which is an





**Figure 4.** (a)–(e) Normalized XANES spectra recorded at (a) Mn, (b) Fe, (c) Co, (d) Ni and (e) Zn K-edges in electrodes based on HEO (solid lines) and (dashed lines) mcHEO NFs after 50th charge (light grey), 50th discharge (light grey) and 750/650 cycles (dark grey, for HEO/mcHEO, respectively). (f)–(j) FT of the EXAFS for all metal K-edge in HEO-electrodes after 50th charge (light grey), 50th discharge (light grey) and 750 cycles (dark grey) compared with metal foil and/or oxide standards for (f) Mn, (g) Fe, (h) Co, (i) Ni and (j) Zn K-edges. All spectra are translated vertically for easier comparison. (k), (l) Average oxidation state of iron, cobalt and nickel in (k) HEO and (l) mcHEO anodes. (m) Average amount of iron, cobalt and nickel to  $\text{Fe}^0$ ,  $\text{Co}^0$  and  $\text{Ni}^0$  accumulated per cycle.

indication of a higher oxidized system. In the Ni  $2p$  spectral region (Fig. 3d), the  $2p_{3/2}$  peaks of  $\text{Ni}^{2+}$  ions in  $\text{NiO}$  oxide and  $\text{Ni}(\text{OH})_2$  hydroxide environment are observed at 854.6 and 855.6 eV, respectively.<sup>139,140</sup> The lower-BE peaks are shifted by +0.6 eV for  $\text{HEO}_{\text{LL}}$  NFs, and those at higher BEs by +1.2 eV for both HEO and  $\text{HEO}_{\text{LL}}$  NFs. These latter, due to the large difference in BE, are more reasonably assigned to a multiplet splitting of Ni  $2p$  lines of  $\text{Ni}^{2+}$  ions in pure  $\text{NiO}$ , rather than in  $\text{Ni}(\text{OH})_2$ -environment.<sup>141</sup> In the Zn  $2p$  spectra region (Fig. 2e), only a couple of peaks, assigned to the  $2p_{3/2}$  and  $2p_{1/2}$  features of zinc atoms, is detected in  $\text{HEO}_{\text{LL}}$  NFs; the Zn  $2p_{3/2}$  peak is centered at 1021.7 eV, which is assigned to  $\text{Zn}^{2+}$  species in  $\text{ZnO}$  oxide environment.<sup>142,143</sup> Interestingly, for mcHEO and HEO NFs, the splitting of these peaks into two components, one above and one below that of the  $\text{HEO}_{\text{LL}}$  NFs, reveals the presence of  $\text{Zn}^{2+}$  species in both hydroxide and pure zinc oxide environment.<sup>142,143</sup>

Taken all together, high resolution XPS studies on TMs reveal that their oxidized character raises in the order  $\text{mcHEO} < \text{HEO} < \text{HEO}_{\text{LL}}$  (i.e. with the effectiveness of the crystallization process), while the surface defectiveness has an opposite trend.

Further insights on the defect concentration on the surface of the investigated materials is achieved analyzing in details the O  $1s$

spectral region (Fig. 3f).<sup>92,97</sup> In particular, the O  $1s$  signal is the result of the superposition of three different features: (i) the peak at *ca.* 529.9 eV the lattice  $\text{O}^{2-}$  ions ( $\text{O}_{\text{L}}$ ) belongs to mixed TM oxides;<sup>142,144–146</sup> (ii) the peak at *ca.* 531.4 eV, commonly attributed to “oxygen vacancies” ( $\text{O}_{\text{V}}$ ),<sup>138,146,147</sup> comes from oxygen atoms in the neighborhood of lattice oxygen vacancies, which according to a recent computational paper<sup>148</sup> are surface  $-\text{OH}$  groups saturating O vacancies;<sup>149</sup> and (iii) the peak at higher BEs arises from the adsorbed or chemisorbed oxygen species, such as  $\text{O}_2$  or  $\text{H}_2$ .<sup>81,92,138</sup> The concentration of  $\text{O}_{\text{V}}$  species decreases from 40.6% in mcHEO NFs<sup>81</sup> to 33.1 and 23.2% in HEO and  $\text{HEO}_{\text{LL}}$  NFs, respectively; the decrease is linearly in  $d_{\text{SHEO}}$ , the larger  $d_{\text{SHEO}}$ , i.e. the higher the oxide crystallinity, the lower the  $\text{O}_{\text{V}}$  concentration. Surprisingly, the anode prepared with the NFs with the lowest concentration of  $\text{O}_{\text{V}}$  on their surface ( $\text{HEO}_{\text{LL}}$ ) outperforms the remaining ones in terms of both high RC and LTS (Figs. 1h, 1i), contrary to the literature reports on the beneficial role played by the  $\text{O}_{\text{V}}$  species in the  $\text{Li}^+$  diffusion and storage.<sup>72,80</sup> This result, in line with the previous finding that lattice defects hinder  $\text{Li}$ -ion diffusion,<sup>71</sup> further confirms that larger particle size, increased crystallinity and proximity to the equilibrium cation distribution are beneficial for the electrochemical performance of the SHEO NFs.

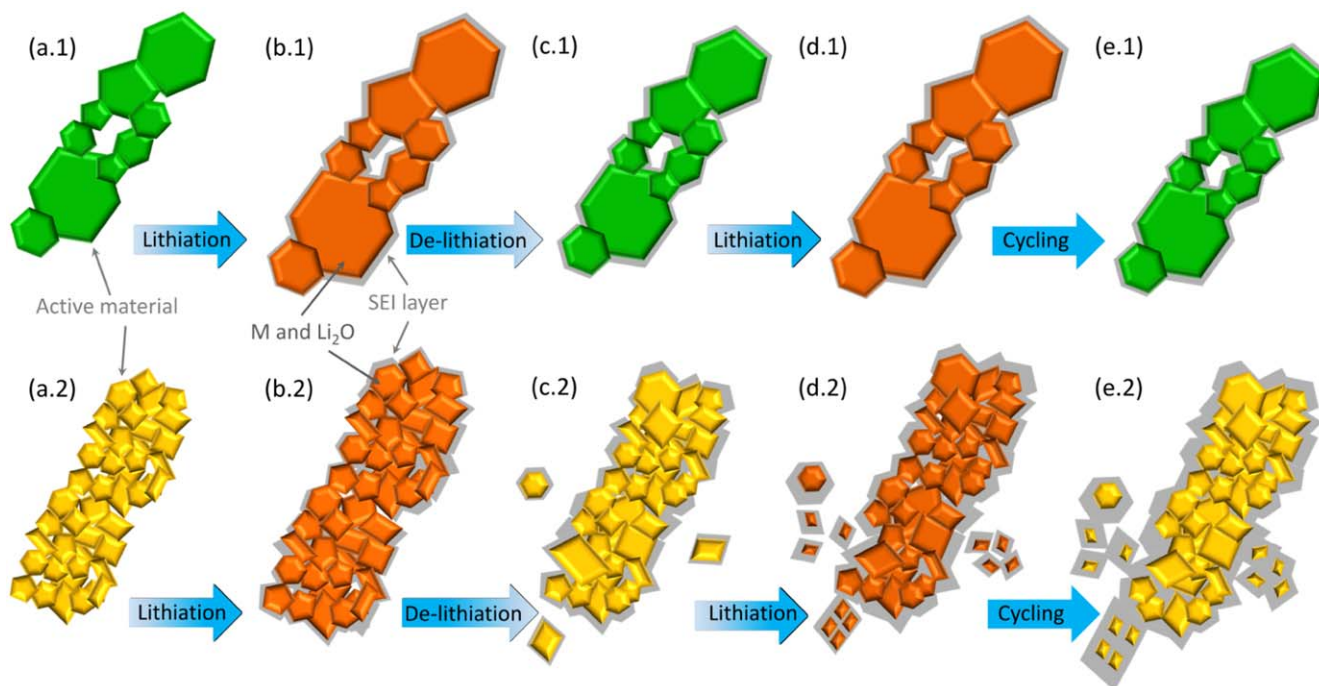


**Figure 5.** Schematic illustration of SEI formation on (top) HEO<sub>LL</sub> and (bottom) mcHEO<sub>LL</sub> NFs (inspired to Ref. 7). In the case of HEO<sub>LL</sub> NFs, a stable SEI layer is formed and the original morphology is retained after several cycles. The mcHEO<sub>LL</sub> NFs, made up of smaller oxide grains, have a greater surface area exposed to electrolyte and SEI forms to a greater extent; besides, small grains tend to aggregate into larger particles that undergo fracture upon prolonged cycling, leading to further growth of layer SEI.

**Charge storage mechanism and structural changes.**—The mechanism of Li<sup>+</sup> storage in anodes based on SHEO NFs calcined under milder conditions has been object of a previous study.<sup>81</sup> What emerges from the XAS study on the *first* charge/discharge cycle of present anodes is that lithiation process is not affected by the variation of the NF calcination conditions. A detailed discussion of the ex situ XAS results can be found in the SM (Figs. S9–S10 and Table S6). Briefly, lithiation progresses via conversion reaction forming metals, lithium insertion and cation migration, leading to Li-driven spinel to rock-salt transition. An in-depth discussion can be found in the SM. In particular, during discharging, manganese, initially present mainly as Mn<sup>4+</sup>/Mn<sup>3+</sup>, partially reduces to Mn<sup>3+</sup>/Mn<sup>2+</sup>; iron, cobalt and nickel, initially present mainly as Fe<sup>3+</sup>, Co<sup>3+</sup>/Co<sup>2+</sup> and Ni<sup>2+</sup>, reduce to Fe<sup>0</sup>, Co<sup>0</sup> and Ni<sup>0</sup> (Table S6), probably forming single-metal nanoclusters<sup>72</sup> or a FeCoNi alloy that develops as a dendritic 3D nano-network penetrating the oxide matrix and provides a highly efficient electron-transfer path;<sup>54</sup> lithium is likely incorporated as Li<sub>2</sub>O nanoclusters<sup>54,72</sup> in the Mn, Fe, Co, Ni, Zn-oxide phase, or atomically dispersed within it.<sup>54</sup> Zn<sup>2+</sup> cations that do not electrochemically participate in the conversion reaction ensure the structure stability. During charging, re-oxidation of Mn, Fe, Co and Ni occurs only partially and to different extents among them. Due to the metastability of the Mn, Fe, Co, Ni, Zn-oxide phase at RT, configurational entropy is not fully restored during re-oxidation<sup>54</sup> and lower-entropy nanodomains are formed within the oxide matrix (see below), in agreement with the literature.<sup>39</sup> This structural modification on a local scale does not deprive the active material of the benefits, in terms of electrochemical performance, deriving from the multiple element approach.<sup>150</sup>

Ex-situ XRD analysis of the HEO electrodes (Fig. S12 and Table S7) reveals that at SOC 2 most of the spinel phase transformed into a rock-salt phase (ca. 80%) and that this transformation is completed at SOC 3; no spinel phase reappears during the first charge and second discharge. Amorphization of the rock-salt phase occurs during the initial discharging (Fig. S12j), as revealed by the strong decrease of the coherence length of rock-salt crystallites (Table S7), probably due to the lack of structural reversibility during

re-oxidation.<sup>24</sup> Moreover, a large amount of lithium carbonate (Li<sub>2</sub>CO<sub>3</sub>), which is part of the SEI layer formed by the decomposition of the electrolyte,<sup>151</sup> is detected in the discharged electrodes (Figs. S11a, S11b and S12d–S12h, Table S7). Its amount increases during charge (from 75 to 90%), and after the second discharge returns to 75%, the same value as after the first discharge, hinting at the stability of the SEI layer. Both of these factors are commonly believed to contribute to the good electrochemical performance of anodes.<sup>37,72,75</sup>

**Long-term cycling stability and causes of capacity fading.**—As mentioned above, during the very *first* charge/discharge cycles, the crystal structure of the active material undergoes severe modifications with loss of long-range order and rearrangement in a different phase. As pointed out by Li et al.,<sup>84</sup> this evolution, alone, does not allow explaining the performance of anode material in terms of RC and LTS.

In order to elucidate the causes of capacity fading, ex situ synchrotron XAS analysis was carried out on HEO- and mcHEO-anodes after a high number of charge/discharge cycles. At the best of the authors' knowledge, no reports focused on this topic are available for high-entropy oxides in the literature. Figures 4a–4e compares the XANES spectra recorded in HEO- and mcHEO-anodes after the 50th charge and 50th discharge and at the end of their life (750 and 650 cycles for HEO- and mcHEO-electrodes, respectively). The comparison with the spectra of the oxide and metal standards is shown in Fig. S13 and the results of the LCF analysis are reported in Table S8. Figures 4f–4j compares FT of the EXAFS for all metal K-edge in HEO-electrodes after 50th charge, 50th discharge and 750 cycles and in metal foil and/or oxide standards. These results prove the reduction of increasing amounts of iron (Figs. 4b, 4g), cobalt (Figs. 4c, 4h) and nickel (Figs. 4d, 4i) to the metallic form. One can speculate that, as a consequence, single-metal nanoclusters<sup>62</sup> coalesce in bigger aggregates or that the metallic FeCoNi 3D nano-network<sup>54</sup> continues to develop during cycling by pervasively penetrating the Mn, Fe, Co, Ni, Zn-oxide matrix, processes which both lead to its progressive depletion of redox-

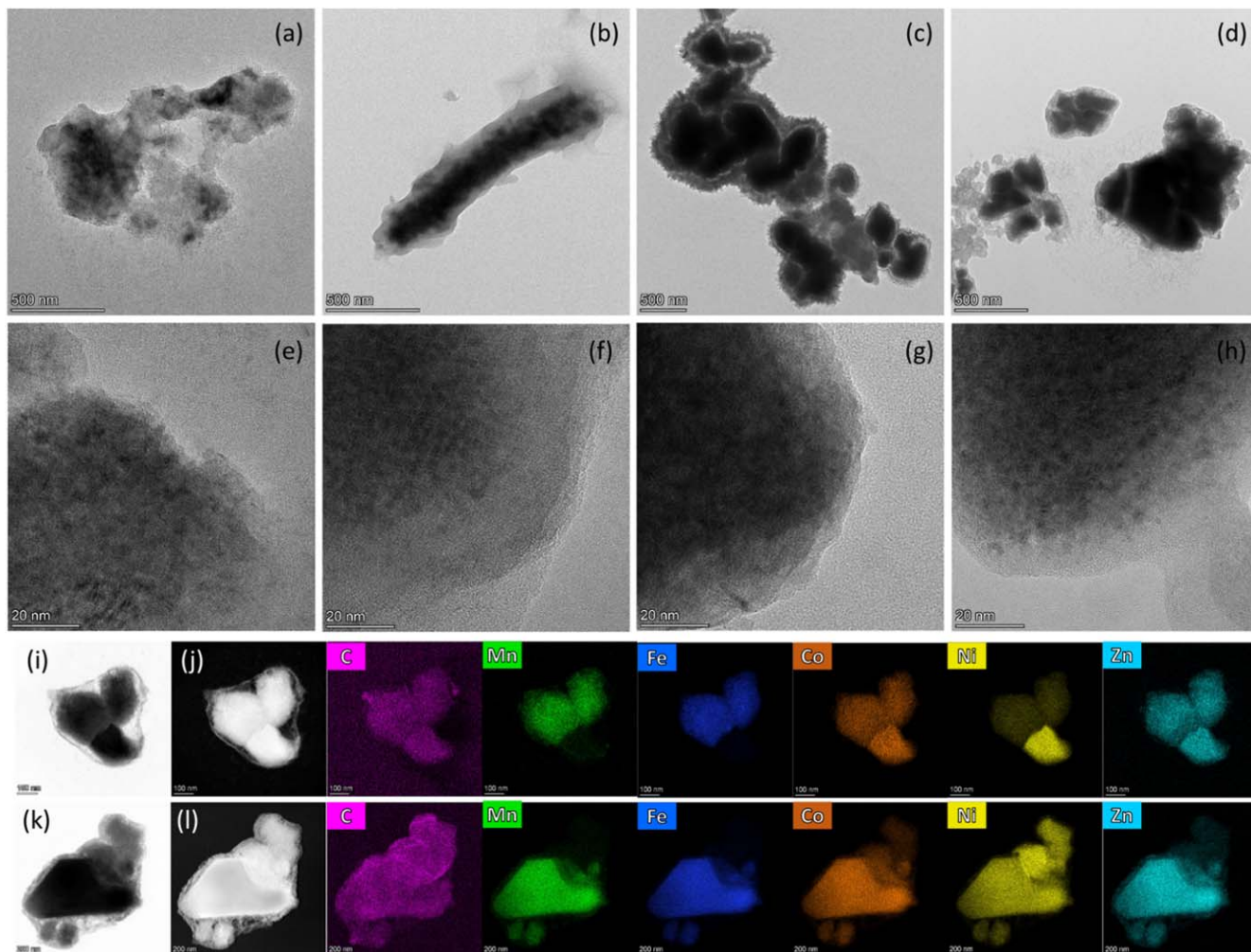


**Figure 6.** (a)–(d) TEM and (e)–(h) HRTEM images of samples (a), (e) mcHEO, (b), (f) mcHEO<sub>LL</sub>, (c), (g) HEO, and (d), (h) HEO<sub>LL</sub>. (i), (k) BF-STEM, and (j), (l) HAADF-STEM images of sample (i), (j) HEO and (k), (l) HEO<sub>LL</sub>, followed by STEM/EDX elemental maps.

active cations. In the case of the HEO-anode, the conversion reaction is reversed to a greater extent than in mcHEO (Fig. S14), as proven by the higher increase in the average oxidation state of Fe, Co and Ni (Figs. 4k, 4l) and the smaller average amount of Fe<sup>0</sup>, Co<sup>0</sup> and Ni<sup>0</sup> accumulated (Fig. 4m). This probably occurs because the less compact architecture of the NFs composed by larger particles (compare Figs. 2a and 2b) promotes accessibility (and re-oxidation) of the FeCoNi clusters,<sup>25,32,98</sup> finally resulting in better capacity retention/smaller capacity fading in HEO-anode.

Based on the picture emerged from the investigation of the physicochemical properties of the pristine active materials in terms of size and crystallinity of the oxide grains and oxidized character of the surface species, above considerations could be extended to HEO<sub>LL</sub>- and mcHEO<sub>LL</sub>-anodes.

**Rate-capability/microstructure relationship.**—It is well known that small-size particles can reduce mechanical stress associated with volume changes during lithiation/de-lithiation, but they are likely to aggregate in larger particles and then fracture,<sup>37</sup> generating new interfaces for the SEI formation.<sup>37,107</sup> Based on literature reports,<sup>37,107</sup> a thick SEI layer is expected to “bury” the active particles and inhibit their participation in electrochemical reactions, causing capacity to fade. This would account for the observed fluctuations in capacity (Fig. 1h). Excessive SEI formation would be the key to also understand the different RC of the investigated NFs (Fig. 1g). At lower rates, higher lithiation capacities are obtained for

thinner (HEO<sub>LL</sub> and mcHEO<sub>LL</sub>) fibers. With increasing rate, the capacity of NFs reduces to different extent. At 2 A g<sup>-1</sup>, the lithiation capacity varies in the same order as  $d_{\text{SHEO}}$  and  $d_{\text{G}}$ , namely mcHEO < mcHEO<sub>LL</sub> < HEO < HEO<sub>LL</sub>. Since capacity is recovered by lowering rate, pulverization of the active material and consequent loss of contact from the binder and the current collector, alone, cannot explain the behavior observed in terms of RC. For the redox reaction to take place, Li-ions and electrons have to go through SEI layer and reach the composited Li<sub>2</sub>O/active material structure. As the diffusion lengths of Li<sup>+</sup> and e<sup>-</sup> (which are the sum of the diffusion lengths relative to each layer) become larger, the portion of active material participating electrochemical reaction becomes smaller.<sup>25,37</sup> The thickening of SEI layer and the internal accumulation of Li<sub>2</sub>O, which is Li-ion conductor, but an electronic insulator,<sup>37</sup> ends up blocking the electron diffusion and hindering the kinetics of the battery. This would explain why at high rates, the variation of the lithiation capacities follows the same trend as the average particle size. Thus, it is expected that, as sketched in Fig. 5, a stable and thinner<sup>152</sup> SEI layer forms over larger oxide grains (Fig. 5a–e.1), while smaller-sized particles (Fig. 5a.2), tend to aggregate (Fig. 5c.2) and break<sup>37,107</sup> (Fig. 5d.2) generating new interfaces and growth of the SEI layer<sup>152</sup> (Fig. 5e.2). In order to verify this hypothesis and shed light on the influence of NF microstructure on the SEI formation, ex situ HRTEM and STEM/EDX measurements were carried out on the long-cycled electrodes. The results, shown in Fig. 6 and S15, fully confirm our expectations. A very thick layer



coats oxide grains in mcHEO electrode (Figs. 6a and S15a, S15b). The layer, containing carbon (see STEM/EDX elemental maps in Figs. 6h–6l and S15k), is constituted by  $\text{Li}_2\text{CO}_3$  (one of the components of SEI layer formed by the decomposition of the electrolyte<sup>151</sup>), as suggested by ex situ XRD and MRS analyses (Fig. S11) and confirmed by electron diffraction (ED) patterns (Figs. S16d, S16f). The relative thickness of the SEI layer progressively decreases with the increase  $d_G$ . In the best performing  $\text{HEO}_{\text{LL}}$  sample, whose structural stability is proved by the identification of rock-salt lattice in the ED pattern (Fig. S16b), the SEI layer forms a relatively thin conformal coating on the oxide grains (Fig. 6d).

Ex-situ elemental mapping further reveals that in cycled  $\text{HEO}$ - and  $\text{HEO}_{\text{LL}}$ -electrodes, zinc is uniformly distributed in all grains, in agreement with its stabilizing role for the structure; the remaining TMs exhibit a non-homogeneous distribution, with coexistence of Ni-rich domains (with some Co and Zn) and Ni-poor domains, in agreement with reports by other authors.<sup>39</sup>

In order to further elucidate the high-rate behavior of the anodes, the kinetics of the lithium insertion/extraction was investigated by CV at different scan rates (from 0.1 to 1 mV s<sup>-1</sup>). As shown in Fig. S16, the CV curves of all anodes except HEO show similar shapes and the peak current ( $i_p$ ) increases with the potential scanning rate ( $v$ ). The relationship between peak current and scan rate,  $i_p = av^b$ , allows establishing the mechanism that controls lithium storage kinetics. When the power law exponent  $b = 0.5$ , the process is completely controlled by diffusion, while when  $b = 1$ , the charge storage is pseudocapacitive; for intermediate  $b$  values both mechanisms contribute.<sup>55,58,75,78,80,82</sup> The value of  $b$ , calculated as the slope of the  $\log(i_p)$  vs  $\log(v)$  plot (Fig. S17a), ranges between 0.59 and 0.80. This indicates that the kinetics of Li-storage in (MnFeCoNiZn)-HEO anodes involves both ion-diffusion and fast surface/subsurface charge transfer reaction.<sup>153</sup> The increase of  $b$  in the order mcHEO (0.59) < mcHEO<sub>LL</sub> (0.64) < HEO<sub>LL</sub> (0.80), which is not in contrast with the guessed SEI thinning,<sup>153</sup> suggests improved surface/subsurface charge transfer and, hence, accounts for the observed enhancement in rate performance (Fig. S17b).<sup>55,58</sup>

## Conclusions

Electrospun high-entropy (Mn,Fe,Co,Ni,Zn) oxide nanofibers to be used as anode active materials in LIBs are produced by adding different metal loads in the precursor solution (19.23 or 38.46 wt%) and varying the calcination conditions (700 °C for 0.5 h, or 700 °C for 2 h and 900 °C for 2 h). In-depth analysis using a combination of analytical techniques reveals that fibers with different morphology, microstructure, crystalline phase, surface composition and electrochemical properties are obtained.

The mechanism of  $\text{Li}^+$  storage, as elucidated by ex situ synchrotron XAS, involves conversion reactions and initial intercalation, accompanied by the transition from spinel to rock-salt, as typical of TM oxides with a spinel structure. The electrochemical performance of the nanofibers strongly depends on their microstructure. The best performance pertains to the fibers ( $\text{HEO}_{\text{LL}}$ ) composed by larger and better-crystallized grains, with more oxidized species and fewer defects on their surface, which exhibit superior rate-capability and long-term stability, delivering 210 mAh g<sup>-1</sup> at a rate of 2 A g<sup>-1</sup>, and capacities as high as 453 mAh g<sup>-1</sup> after 550 cycles at 0.5 A g<sup>-1</sup>.



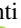



Regardless of the preparation conditions of the fibers, the amount of metallic species formed upon lithiation increases in the order cobalt < iron < nickel. The reverse conversion reaction during charging is reversible to a greater extent for fibers calcined at higher temperature, so they undergo slower capacity fading upon long-term cycling. The superior rate-capability of these fibers has a kinetic origin. Ex-situ TEM images reveal that the tendency to aggregation of smaller-size particles favors the thickening of SEI layer. This increases the length Li-ions and electrons have to diffuse through and hinders the kinetics of the battery, as evidenced by CV measurements at different scan rates.

This study sheds light on the causes of capacity fading upon long-term cycling and demonstrates the huge importance of engineering the microstructure of high-entropy oxides to be used as active anode material in LIBs. The reported results constitute a solid basis for the enhancement of their electrochemical performance via the rational optimization of their preparation conditions.

## Acknowledgments

C.T., M.M. and Y.L. contributed equally to this work. Christoph Erdmann is acknowledged for transmission electron microscopy measurements. Measurements at ELETTRA were supported by the project #20220179. Y. L. acknowledges the fellowship from the China Scholarship Council (CSC). M.G., M.L. and M.M. acknowledge the partial funding from the National Recovery and Resilience Plan (NRRP), Mission 04 Component 2, Investment 1.5—NextGenerationEU, PE2 NEST - Network 4 Energy Sustainable Transition, Spoke 6 Energy Storage. Claudia Triolo (Data curation: Equal; Formal analysis: Equal; Investigation: Equal; Methodology: Equal). Mariam Maisuradze (Data curation: Equal; Formal analysis: Equal; Investigation: Equal; Methodology: Equal). Yanchen Liu (Data curation: Equal; Formal analysis: Equal; Investigation: Equal; Methodology: Equal; Writing—original draft: Supporting). Min Li (Data curation: Supporting; Investigation: Supporting). Gieole Pagot (Formal analysis: Equal; Investigation: Equal; Writing—original draft: Supporting). Alessandro Ponti (Formal analysis: Equal; Software: Lead; Writing—original draft: Equal; Writing—review & editing: Equal). Vito Di Noto (Formal analysis: Equal; Investigation: Equal; Supervision: Equal). Giuliana Aquilanti (Data curation: Supporting; Investigation: Supporting). Nicola Pinna (Resources: Equal; Supervision: Equal; Writing—review & editing: Equal). Marco Giorgetti (Conceptualization: Equal; Funding acquisition: Equal; Methodology: Equal; Supervision: Equal; Writing—review & editing: Supporting). Saveria Santangelo (Conceptualization: Equal; Formal analysis: Equal; Funding acquisition: Equal; Resources: Equal; Supervision: Lead; Visualization: Lead; Writing—original draft: Lead; Writing—review & editing: Lead). The data that support the plots in this paper and other findings of this study are available from the corresponding authors upon reasonable request. There are no conflicts to declare.

## ORCID

Claudia Triolo  <https://orcid.org/0000-0001-9263-7786>  
 Mariam Maisuradze  <https://orcid.org/0000-0002-1498-1706>  
 Gieole Pagot  <https://orcid.org/0000-0002-4015-6670>  
 Alessandro Ponti  <https://orcid.org/0000-0002-1445-5351>  
 Vito Di Noto  <https://orcid.org/0000-0002-8030-6979>  
 Nicola Pinna  <https://orcid.org/0000-0003-1273-803X>  
 Marco Giorgetti  <https://orcid.org/0000-0001-7967-8364>  
 Saveria Santangelo  <https://orcid.org/0000-0003-1732-248X>

## References

- R. Wang, W. Cui, F. Chua, and F. Wu, *J. Energy Chem.*, **48**, 145 (2020).
- F. Wu, Y.-X. Yuan, X.-B. Cheng, Y. Bai, Y. Li, C. Wu, and Q. Zhang, *Energy Storage Mater.*, **15**, 148 (2018).
- H. Liu, X.-B. Cheng, R. Xu, X.-Q. Zhang, C. Yan, J.-Q. Huang, and Q. Zhang, *Adv. Energy Mater.*, **9**, 1902254 (2019).
- X. B. Cheng, T. Z. Hou, R. Zhang, H. J. Peng, C. Z. Zhao, J. Q. Huang, and Q. Zhang, *Adv. Mater.*, **28**, 2888 (2016).
- X. B. Cheng, R. Zhang, C. Z. Zhao, and Q. Zhang, *Chem. Rev.*, **117**, 10403 (2017).
- X. B. Cheng, C. Yan, H.-J. Peng, J.-Q. Huang, S.-T. Yang, and Q. Zhang, *Energy Storage Mater.*, **10**, 199 (2018).
- X. Xu, S. Wang, H. Wang, C. Hu, Y. Jin, J. Liu, and H. Yan, *J. Energy Chem.*, **27**, 513 (2018).
- J. Zheng, T. Tang, Q. Zhao, X. Liu, Y. Deng, and L. A. Archer, *ACS Energy Lett.*, **4**, 1349 (2019).
- L. Xuyan, Z. Xinjie, and P. Deng, *R. Soc. Open Sci.*, **5**, 172370 (2018).
- M. Winter, J. O. Besenhard, M. E. Spahr, and P. Novak, *Adv. Mater.*, **10**, 725 (1998).
- X. Su, Q. Wu, J. Li, X. Xiao, A. Lott, W. Lu, B. W. Sheldon, and J. Wu, *Adv. Energy Mater.*, **4**, 375 (2013).
- L. Liu, J. Lyu, T. Li, and T. Zhao, *Nanoscale*, **8**, 701 (2016).
- F. H. Du, K. X. Wang, and J. S. Chen, *J. Mater. Chem. A*, **4**, 32 (2016).
- X. Fan, D. Deng, Y. Li, and Q. H. Wu, *Curr. Mater. Sci.*, **16**, 18 (2023).

15. H. Zhang and H. Xu, *Solid State Ion.*, **263**, 23 (2014).
16. X. D. Huang, F. Zhang, X. F. Gan, Q. A. Huang, J. Z. Yang, P. T. Laic, and W. M. Tang, *RSC Adv.*, **8**, 5189 (2018).
17. S. Y. Huang, L. Kavan, I. Exnar, and M. Grätzel, *J. Electrochem. Soc.*, **142**, L142 (1995).
18. Z. Chen, I. Belharouak, Y. K. Sun, and K. Amine, *Adv. Funct. Mater.*, **23**, 959 (2013).
19. T. Ohzuku, A. Ueda, and N. Yamamoto, *J. Electrochem. Soc.*, **142**, 1431 (1995).
20. D. Bresser, E. Paillard, M. Copley, P. Bishop, M. Winter, and S. Passerini, *J. Power Sources*, **219**, 217 (2012).
21. B. N. Loeffler, D. Bresser, S. Passerini, and M. Copley, *Platinum Met. Rev.*, **59**, 34 (2015).
22. I. A. Courtney, *J. Electrochem. Soc.*, **144**, 2943 (1997).
23. F. Belliard and J. Irvine, *J. Power Sources*, **97**, 219 (2001).
24. J. Read, D. Foster, J. Wolfenstine, and W. Behl, *J. Power Sources*, **96**, 277 (2001).
25. C. J. Pelliccione, Y. Ding, E. V. Timofeeva, and C. U. Segre, *J. Electrochem. Soc.*, **162**, A1935 (2015).
26. D. Bresser, S. Passerini, and B. Scrosati, *Energy Environ. Sci.*, **9**, 3348 (2016).
27. P. L.-S. G. Poizot, S. Laruelle, S. Grugeon, L. Dupont, and J. M. Tarascon, *Nature*, **407**, 496 (2000).
28. J. Cabana, L. Monconduit, D. Larcher, and M. R. Palacin, *Adv. Mater.*, **22**, E170 (2010).
29. N. Nitta and G. Yushin, *Part. Part. Syst. Charact.*, **31**, 317 (2014).
30. Z. M. Cui, L. Y. Jiang, W. G. Song, and Y. G. Guo, *Chem. Mater.*, **21**, 1162 (2009).
31. B. Varghese, M. Reddy, Z. Yanwu, C. S. Lit, T. C. Hoong, G. Subba Rao, B. Chowdari, A. T. S. Wee, C. T. Lim, and C. H. Sow, *Chem. Mater.*, **20**, 3360 (2008).
32. P. Lavela, J. L. Tirado, M. Womes, and J. C. Jumas, *J. Electrochem. Soc.*, **156**, A589 (2009).
33. S. Fang, D. Bresser, and S. Passerini, *Adv. Energy Mater.*, **10**, 1902485 (2020).
34. S. H. Yu, S. H. Lee, D. J. Lee, Y. E. Sung, and T. Hyeon, *Small*, **12**, 2146 (2016).
35. D. Wu, J. Song, Y. Ji, Q. Tian, Z. Sui, J. Chen, and L. Yang, *J. Electroanalytical Chem.*, **895**, 115531 (2021).
36. S. Fang, D. Bresser, and S. Passerini, "Transition metal oxide anodes for electrochemical energy storage in lithium-and sodium-ion batteries." In *Transition Metal Oxides for Electrochemical Energy Storage*, ed. J. Nanda and V. Augustyn (2022), Ch 4. (Wiley, New York).
37. S. H. Lee et al., *Nano Lett.*, **13**, 4249 (2013).
38. S. Balamurugan, N. Naresh, I. Prakash, and N. Satyanarayana, *Appl. Surf. Sci.*, **535**, 147677 (2021).
39. C. Y. Huang et al., *Chem. Eng. J.*, **420**, 129838 (2021).
40. M. K. Rath and K. T. Lee, *Ceram. Int.*, **41**, 10878 (2015).
41. M. Fiore, G. Longoni, S. Santangelo, F. Pantò, S. Stelitano, P. Frontera, P. Antonucci, and R. Ruffo, *Electrochim. Acta*, **269**, 367 (2018).
42. B. Petrovičová, W. Xu, M. G. Musolino, F. Pantò, S. Patanè, N. Pinna, S. Santangelo, and C. Triolo, *Appl. Sci.*, **12**, 5965 (2022).
43. Y. Liu, J. Hou, C. Cheng, F. Cheng, T. Su, Y. Miao, C. Ma, and X. Wang, *Ceram. Int.*, **49**, 21546 (2023).
44. S. Goriparti, E. Miele, F. De Angelis, E. Di Fabrizio, R. P. Zaccaria, and C. Capiglia, *J. Power Sources*, **257**, 421 (2014).
45. R. Xia et al., *Adv. Energy Mater.*, **12**, 2102972 (2022).
46. N. S. Hudak, "Nanostructured electrode materials for lithium-ion batteries." In *Lithium-Ion Batteries 57* (Elsevier, Amsterdam) (2014).
47. B. Cantor, I. T.-H. Chang, P. Knight, and A. J.-B. Vincent, *Mater. Sci. Eng. A*, **375**, 213 (2004).
48. J. W. Yeh, S. K. Chen, S. J. Lin, J. Y. Gan, T. S. Chin, T. T. Shun, C. H. Tsau, and S. Y. Chang, *Adv. Eng. Mater.*, **6**, 299 (2004).
49. J. Zhou, J. Zhang, F. Zhang, B. Niu, L. Lei, and W. Wang, *Ceramics Int.*, **44**, 22014 (2018).
50. C. M. Rost, E. Sachet, T. Borman, A. Moballeghe, E. C. Dickey, D. Hou, J. L. Jones, S. Curtarolo, and J. P. Maria, *Nature Commun.*, **6**, 8485 (2015).
51. T. Jin, X. Sang, R. R. Unocic, R. T. Kinch, X. Liu, J. Hu, H. Liu, and S. Dai, *Adv. Mater.*, **30**, 1707512 (2018).
52. S. Akrami, P. Edalati, M. Fuji, and K. Edalati, *Mater. Sci. Eng. R*, **146**, 100644 (2021).
53. R. Z. Zhang, F. Gucci, H. Zhu, K. Chen, and M. J. Reece, *Inorganic Chem.*, **57**, 13027 (2018).
54. K. Wang et al., *Nature Commun.*, **14**, 1487 (2023).
55. K. Du, Y. Liu, Y. Yang, F. Cui, J. Wang, M. Han, J. Su, J. Wang, X. Han, and Y. Hu, *Adv. Mater.*, **35**, 2301538 (2023).
56. M. Fu, X. Ma, K. Zhao, X. Li, and D. Su, *Science*, **24**, 102177 (2021).
57. Z. Y. Gu et al., *Adv. Mater.*, **36**, 2400690 (2024).
58. Y. N. Liu et al., *Angew. Chem.*, **63**, e202316925 (2024).
59. Q. Wang, A. Sarkar, Z. Li, Y. Lu, L. Velasco, S. S. Bhattacharya, T. Brezesinski, H. Hahn, and B. Breitung, *Electrochem. Commun.*, **100**, 121 (2019).
60. D. Bérardan, S. Franger, A. K. Meena, and N.-J. Dragoe, *Mater. Chem. A*, **4**, 9536 (2016).
61. A. Sarkar et al., *Nature Commun.*, **9**, 3400 (2018).
62. Q. Wang et al., *Energy Environ. Sci.*, **12**, 2433 (2019).
63. Y. Chen, H. Fu, Y. Huang, L. Huang, X. Zheng, Y. Dai, Y. Huang, and W. Luo, *ACS Mater. Lett.*, **3**, 160 (2020).
64. E. Lokcu, C. Toparli, and M. Anik, *ACS Appl. Mater. Interfaces*, **12**, 23860 (2020).
65. M. Kheradmandfard, H. Minouei, N. Tsvetkov, A. K. Vayghan, S. F. Kashani-Bozorg, G. Kim, S. I. Hong, and D. E. Kim, *Mater. Chem. Phys.*, **262**, 124265 (2021).
66. S. Y. Wang, T. Y. Chen, C. H. Kuo, C. C. Lin, S. C. Huang, M. H. Lin, C. C. Wang, and H. Y. Chen, *Mater. Chem. Phys.*, **274**, 125105 (2021).
67. H. Chen, N. Qiu, B. Wu, Z. Yang, S. Sun, and Y. Wang, *RSC Adv.*, **9**, 28908 (2019).
68. N. Qiu, H. Chen, Z. Yang, S. Sun, Y. Wang, and Y. Cui, *J. Alloys Compounds*, **777**, 767 (2019).
69. P. Ghigna et al., *ACS Appl. Mater. Interfaces*, **12**, 50344 (2020).
70. J. Su, Z. Cao, Z. Jiang, G. Chen, Y. Zhu, L. Wang, and G. Li, *Int. J. Appl. Ceram. Technol.*, **202219**, 2004 (2022).
71. C. Triolo, W. Xu, B. Petrovičová, N. Pinna, and S. Santangelo, *Adv. Funct. Mater.*, **32**, 220289 (2022).
72. S. Hou et al., *Adv. Funct. Mater.*, **34**, 2307923 (2024).
73. H. Minouei, N. Tsvetkov, M. Kheradmandfard, J. Han, D. E. Kim, and S. I. Hong, *J. Power Sources*, **549**, 232041 (2022).
74. T. X. Nguyen, J. Patra, J. K. Chang, and J. M. Ting, *J. Mater. Chem. A*, **8**, 18963 (2020).
75. D. Wang, S. Jiang, C. Duan, J. Mao, Y. Dong, K. Dong, Z. Wang, S. Luo, Y. Liu, and X. Qi, *J. Alloys Comp.*, **844**, 156158 (2020).
76. T. Y. Chen et al., *J. Mater. Chem. A*, **8**, 21756 (2020).
77. B. Xiao, G. Wu, T. Wang, Z. Wei, Y. Sui, B. Shen, J. Qi, F. Wei, and J. Zheng, *Nano Energy*, **95**, 106962 (2022).
78. H. Chen, N. Qiu, B. Wu, Z. Yang, S. Sun, and Y. Wang, *RSC Adv.*, **10**, 9736 (2020).
79. B. Xiao et al., *Ceram. Int.*, **47**, 33972 (2021).
80. B. Xiao et al., *ACS Appl. Mater. Interfaces*, **15**, 2792 (2023).
81. C. Triolo et al., *Small*, **19**, 2304585 (2023).
82. Y. Zheng, X. Wu, X. Lan, and R. Hu, *Processes*, **2021**, **10**, 49 (2021).
83. T. X. Nguyen, C. C. Tsai, J. Patra, O. Clemens, J. K. Chang, and J. M. Ting, *Chem. Eng. J.*, **430**, 132658 (2022).
84. J. Li et al., *Nature Commun.*, **10**, 2224 (2019).
85. M. Abdollahifar, P. Molaiyan, M. Perovic, and A. Kwade, *Energies*, **15**, 8791 (2022).
86. J. Kim, S. M.-N. Jeghan, and G. Lee, *Microporous Mesoporous Mater.*, **305**, 110325 (2020).
87. S. Cavaliere, (2015), Ed. *Electrospinning for Advanced Energy and Environmental Applications* (CRC Press, Boca Raton, FL).
88. Q. Liu, J. Zhu, L. Zhang, and Y. Qiu, *Renew. Sust. Energy Rev.*, **81**, 1825 (2018).
89. S. Santangelo, *Appl. Sci.*, **9**, 1049 (2019).
90. Y. Xing, W. Dan, Y. Fan, and X. A. Li, *J. Mater. Sci. Technol.*, **103**, 215 (2022).
91. W. Zhao, F. Yang, Z. Liu, H. Chen, Z. Shao, X. Zhang, K. Wang, and L. Xue, *Ceram. Int.*, **47**, 29379 (2021).
92. C. Triolo, S. Schweidler, L. Lin, G. Pagot, V. Di Noto, B. Breitung, and S. Santangelo, *Energy Adv.*, **2**, 667 (2023).
93. J. M. Deitzel, J. Kleinmeyer, D. E.-A. Harris, and N. B. Tan, *Polymer*, **42**, 261 (2001).
94. G. Korotcenkov, *Nanomater.*, **11**, 1544 (2021).
95. A. Senthamizhan, B. Balusamy, Z. Aytac, and T. Uyar, *CrystEngComm*, **18**, 6341 (2016).
96. C. Triolo, K. Moulae, A. Ponti, G. Pagot, V. Di Noto, N. Pinna, G. Neri, and S. Santangelo, *Adv. Funct. Mater.*, **34**, 2306375 (2024).
97. A. Ponti, C. Triolo, B. Petrovičová, A. M. Ferretti, G. Pagot, W. Xu, V. Di Noto, N. Pinna, and S. Santangelo, *Phys. Chem. Chem. Phys.*, **25**, 2212 (2023).
98. C. Vidal-Abarca, P. Lavela, and J. L. Tirado, *J. Phys. Chem. C*, **114**, 12828 (2010).
99. A. Mullaliu, J. Asenbauer, G. Aquilanti, S. Passerini, and M. Giorgetti, *Small Methods*, **4**, 1900529 (2020).
100. L. Lutterotti and P. Scardi, *J. Appl. Cryst.*, **23**, 246 (1990).
101. D. Briggs and M. P. Seah, *Practical Surface Analysis: Auger and X-ray Photoelectron Spectroscopy* (Wiley, New York) (1990).
102. D. A. Shirley, *Phys. Rev. B*, **5**, 4709 (1972).
103. G. Aquilanti et al., *J. Phys. D: Appl. Phys.*, **50**, 074001 (2017).
104. B. Ravel and M. Newville, *J. Synchrotron Rad.*, **12**, 537 (2005).
105. M. Bijelić, X. Liu, Q. Sun, A. B. Djurišić, M. H. Xie, A. M. Ng, C. Suchomski, I. Djerdj, Ž. Skoko, and J. Popović, *J. Mater. Chem. A*, **3**, 14759 (2015).
106. G. Zhang, L. Yu, H. B. Wu, H. E. Hoster, and X. W. Lou, *Adv. Mater.*, **24**, 4609 (2012).
107. H. Song, L. Shen, and C.-J. Wang, *Mater. Chem. A*, **2**, 20597 (2014).
108. F. Liu, M. Yu, X. Chen, J. Li, H. Liu, and F. Cheng, *Chinese J. Catal.*, **43**, 122 (2022).
109. Q. Hu, Z. Wang, X. Huang, Y. Qin, H. Yang, X. Ren, Q. Zhang, J. Liu, and C. He, *Energy Environ. Sci.*, **13**, 5097 (2020).
110. G. Binitha, M. S. Soumya, A. A. Madhavan, P. Praveen, A. Balakrishnan, K. R.-V. Subramanian, M. V. Reddy, S. V. Nair, A. S. Nair, and N. Sivakumar, *J. Mater. Chem. A*, **1**, 11698 (2013).
111. Y. Li, H. Zhang, X. Zhang, L. Wei, Y. Zhang, G. Hai, and Y. Sun, *J. Mater. Sci.: Mater. in Electronics*, **30**, 15734 (2019).
112. D. Hu, R. Wang, P. Du, G. Li, Y. Wang, D. Fan, and X. Pan, *Ceram. Int.*, **48**, 6549 (2021).
113. F. Pantò, Z. Dahrouch, A. Saha, S. Patanè, S. Santangelo, and C. Triolo, *Appl. Surf. Sci.*, **557**, 149830 (2021).
114. X. Yin, J. Huang, Z. Pu, J. Li, H. Feng, X. Wang, and Y. Wang, *Ceram. Int.*, **47**, 17167 (2021).

115. S. W. Oh, H. J. Bang, Y. C. Bae, and Y. K. Sun, *J. Power Sources*, **173**, 502 (2007).
116. F. M. Courtel, H. Duncan, Y. Abu-Lebdeh, and I. J. Davidson, *J. Mater. Chem.*, **21**, 10206 (2011).
117. F. Mou, J. G. Guan, W. Shi, Z. Sun, and S. Wang, *Langmuir*, **26**, 15580 (2010).
118. C. Wei, Z. Feng, G. G. Scherer, J. Barber, Y. Shao-Horn, and Z. J. Xu, *Adv. Mater.*, **29**, 1606800 (2017).
119. S. Paul, M. A. Rahman, S. B. Sharif, J. H. Kim, S. E.-T. Siddiqui, and M. A.-M. Hossain, *Nanomater.*, **12**, 2034 (2022).
120. J. Dąbrowa, M. Stygar, A. Mikula, A. Knapik, K. Mroczka, W. Tejchman, M. Danielewski, and M. Martin, *Mater. Lett.*, **216**, 32 (2018).
121. A. Mao, F. Quan, H. Z. Xiang, Z. G. Zhang, K. Kuramoto, and A. L. Xia, *J. Mol. Struct.*, **1194**, 11 (2019).
122. M. Stygar, J. Dąbrowa, M. Moździerz, M. Zajusz, W. Skubida, K. Mroczka, K. Berent, K. Świerczek, and M. Danielewski, *J. Eur. Ceram. Soc.*, **40**, 1644 (2020).
123. B. Liang, Y. Ai, Y. Wang, C. Liu, S. Ouyang, and M. Liu, *Materials*, **13**, 5798 (2020).
124. A. Kumar, G. Sharma, A. Aftab, and M. I. Ahmad, *J. Eur. Ceram. Soc.*, **40**, 3358 (2020).
125. B. Cheng et al., *Mater. Today Adv.*, **8**, 100102 (2020).
126. M. Fracchia, P. Ghigna, T. Pozzi, U. Anselmi Tamburini, V. Colombo, L. Braglia, and P. Torelli, *J. Phys. Chem. Lett.*, **11**, 3589 (2020).
127. H. D. Lutz, B. Müller, and H. J. Steiner, *J. Solid State Chem.*, **90**, 54 (1991).
128. Z. Wang, R. T. Downs, V. Pischedda, R. Shetty, S. K. Saxena, C. S. Zha, Y. S. Zhao, D. Schiferl, and A. Waskowska, *Phys. Rev. B*, **68**, 094101 (2003).
129. V. D'Ippolito, G. B. Andreozzi, D. Bersani, and P. P. Lottici, *J. Raman Spectrosc.*, **46**, 1255 (2015).
130. B. Nandan, M. C. Bhatnagar, and S. C. Kashyap, *J. Phys. Chem. Solids*, **129**, 298 (2019).
131. M. A. Laguna-Bercero, M. L. Sanjuán, and R. I. Merino, *J. Phys.: Condensed Matter*, **19**, 186217 (2007).
132. Z. Ž. Lazarević, Č. Jovalekić, A. Milutinović, D. Sekulić, V. N. Ivanovski, A. Rečnik, B. Cekić, and N. Ž. Romčević, *J. Appl. Phys.*, **113**, 187221 (2013).
133. R. S. Yadav, I. Kuřitka, J. Vilcakova, J. Havlicka, J. Masilko, L. Kalina, J. Tzacz, J. Švec, V. Enev, and M. Hajdúchová, *Adv. Nat. Sci.: Nanosci. Nanotechnol.*, **8**, 045002 (2017).
134. B. Talluri, K. Yoo, and J. Kim, *J. Environ. Chem. Eng.*, **10**, 106932 (2022).
135. J. F. Moulder, W. F. Stickle, P. E. Sobol, and K. D. Bomben, *Handbook of X-ray Photoelectron Spectroscopy: A Reference Book of Standard Spectra for Identification and Interpretation of XPS Data, Physical Electronics Division* (Perkin-Elmer Corporation, Eden Prairie, 55344 - Minnesota, USA) (1992).
136. R. O. Ansell, T. Dickinson, and A. F. Povey, *Corrosion Sci.*, **18**, 245 (1978).
137. G. C. Stevens and T. Edmonds, *J. Less-Comm. Met.*, **54**, 321 (1977).
138. B. J. Tan, K. J. Klabunde, and P. M. Sherwood, *J. Am. Chem. Soc.*, **113**, 855 (1991).
139. K. S. Kim and N. Winograd, *Surf. Sci.*, **43**, 625 (1974).
140. P. Lorenz, J. Finster, G. Wendt, J. V. Salyn, E. K. Žumadilov, and V. I. Nefedov, *J. Electron Spectrosc. Relat. Phenomena*, **16**, 267 (1979).
141. M. C. Biesinger, L. W. M. Lau, A. R. Gerson, and R. S. C. Smart, *Phys. Chem. Chem. Phys.*, **14**, 2434 (2012).
142. B. R. Strohmeier and D. M. Hercules, *J. Catal.*, **86**, 266 (1984).
143. G. Deroubaix and P. Marcus, *Surf. Interface Analysis*, **18**, 39 (1992).
144. J. P. Bonnelle, J. Grimblot, and A. D'Huysser, *J. Electron Spectrosc. Relat. Phenomena*, **7**, 151 (1975).
145. V. Nefedov, D. Gati, B. Dzhurinskii, N. Sergushin, and Y. V. Salyn, *Zh. Neorg. Khim.*, **20**, 2307 (1975).
146. G. Pagot, M. C. Cassani, F. Gambassi, B. Ballarin, D. Nanni, M. Coi, D. Barreca, E. Boanini, and V. D. Noto, *Surf. Sci. Spectra*, **29**, 024007 (2022).
147. J. Haber, J. Stoch, and L. Ungier, *J. Electron Spectrosc. Relat. Phenomena*, **9**, 459 (1976).
148. T. J. Frankcombe and Y. Liu, *Chem. Mater.*, **35**, 5468 (2023).
149. L. Bigiani, A. Gasparotto, G. Carraro, C. Maccato, and D. Barreca, *Surf. Sci. Spectra*, **25**, 024005 (2018).
150. T. G.-U. Ghobadi, M. Kunduraci, and E. Yilmaz, *J. Alloys Comp.*, **730**, 96 (2018).
151. L. Alzate-Vargas, S. M. Blau, E. W.-C. Spotte-Smith, S. Allu, K. A. Persson, and J. L. Fattebert, *J. Phys. Chem. C*, **125**, 18588 (2021).
152. D. Shin, S. Chae, S. Park, B. Seo, and W. Choi, *NPG Asia Mater.*, **15**, 54 (2023).
153. G. Z. Chen, *Prog. Nat. Sci.: Mater. Int.*, **31**, 792 (2021).